Bioactive Materials 11 (2022) 15–31

Contents lists available at ScienceDirect

Bioactive Materials

journal homepage: www.keaipublishing.com/en/journals/bioactive-materials

Construction of a niche-specific spinal white matter-like tissue to promote directional axon regeneration and myelination for rat spinal cord injury repair

Bi-Qin Lai [a,b,c,d,f,**,1], Yu-Rong Bai [a,1], Wei-Tao Han [b], Bao Zhang [b], Shu Liu [e], Jia-Hui Sun [a], Jia-Lin Liu [a], Ge Li [a], Xiang Zeng [a,b,c,f], Ying Ding [a,b,f], Yuan-Huan Ma [a], Ling Zhang [g], Zheng-Hong Chen [g], Jun Wang [h], Yuan Xiong [h], Jin-Hua Wu [h], Qi Quan [i], Ling-Yan Xing [f], Hong-Bo Zhang [b], Yuan-Shan Zeng [a,b,c,d,f,*]

[a] Key Laboratory for Stem Cells and Tissue Engineering (Sun Yat-sen University), Ministry of Education, Guangzhou, 510080, China
[b] Department of Histology and Embryology, Zhongshan School of Medicine, SunYat-sen University, Guangzhou, 510080, China
[c] Institute of Spinal Cord Injury, Sun Yat-sen University, Guangzhou, 510120, China
[d] Co-innovation Center of Neuroregeneration, Nantong University, Nantong, 226001, China
[e] Department of Anatomy, Anhui Medical University, Hefei, 230032, China
[f] Guangdong Provincial Key Laboratory of Brain Function and Disease, Zhongshan School of Medicine, Sun Yat-sen University, Guangzhou, 510080, China
[g] Department of Geriatrics, The First Affiliated Hospital, Sun Yat-sen University, Guangzhou, 510080, China
[h] Physiotherapy Department, Guangdong Work Injury Rehabilitation Hospital, Guangzhou, China
[i] Department of Orthopedic Surgery, Key Laboratory of Musculoskeletal Trauma &War Injuries PLA, Beijing Key Lab of Regenerative Medicine in Orthopedics, The 4th Medical Centre, Chinese PLA General Hospital, Beijing, China

ARTICLE INFO

Keywords:
Extracellular matrix
Oligodendroglial lineage cells
White matter-like tissue
Directional axon regeneration
Spinal cord injury

ABSTRACT

Directional axon regeneration and remyelination are crucial for repair of spinal cord injury (SCI), but existing treatments do not effectively promote those processes. Here, we propose a strategy for construction of niche-specific spinal white matter-like tissue (WMLT) using decellularized optic nerve (DON) loaded with neurotrophin-3 (NT-3)-overexpressing oligodendrocyte precursor cells. A rat model with a white matter defect in the dorsal spinal cord of the T10 segment was used. The WMLT transplantation group showed significant improvement in coordinated motor functions compared with the control groups. WMLT transplants integrated well with host spinal cord white matter, effectively addressing several barriers to directional axonal regeneration and myelination during SCI repair. In WMLT, laminin was found to promote development of oligodendroglial lineage (OL) cells by binding to laminin receptors. Interestingly, laminin could also guide linear axon regeneration via interactions with specific integrins on the axon surface. The WMLT developed here utilizes the unique microstructure and bioactive matrix of DON to create a niche rich in laminin, NT-3 and OL cells to achieve significant structural repair of SCI. Our protocol can help to promote research on repair of nerve injury and construction of neural tissues and organoids that form specific cell niches.

1. Introduction

A primary challenge to repair of spinal cord injury (SCI) is a hostile microenvironment at the site of injury that does not support nerve regeneration [1,2]. Although attempts have been made to modify the microenvironment to increase regeneration of neuronal axons, failure of directional axon growth and myelination continues to inhibit progress

Peer review under responsibility of KeAi Communications Co., Ltd.
* Corresponding author. Department of Histology and Embryology Zhongshan School of Medicine Sun Yat-sen University, 74# Zhongshan 2nd Road, Guangzhou, 510080, China.
** Corresponding author. Key Laboratory for Stem Cells and Tissue Engineering, Ministry of Education, Sun Yat-sen University, 74# Zhongshan 2nd Road, Guangzhou, 510080, China.
E-mail addresses: laibqin@mail.sysu.edu.cn (B.-Q. Lai), zengysh@mail.sysu.edu.cn (Y.-S. Zeng).
[1] These authors contributed equally to this manuscript.

https://doi.org/10.1016/j.bioactmat.2021.10.005
Received 26 July 2021; Received in revised form 29 September 2021; Accepted 3 October 2021
Available online 20 October 2021

because they are required for functional spinal cord repair [3–5].

Several studies have attempted to use oligodendrocytes derived from transplanted stem cells for SCI repair, demonstrating that regenerated axonal myelination can restore some degree of motor function [6–8]. However, stem cells directly transplanted into injured spinal cord do not always differentiate, and ensuring efficient oligodendrocyte differentiation can be challenging [6,9]. One strategy to circumvent this uncertainty employs *in vitro* pre-induction of stem cells into oligodendrocyte precursor cells (OPCs) [10,11]. OPCs can differentiate into mature oligodendrocytes engineered to overexpress exogenous neurotrophic factors, including glial cell-derived neurotrophic factor, ciliary neurotrophic factor, neurotrophin-3 (NT-3), and others, to promote development of a microenvironment that is supportive of nerve regeneration and myelination [10–13].

Several studies have demonstrated that NT-3 can promote corticospinal tract (CST) axon regeneration and increase oligodendrocyte myelination activity [14–16]. We hypothesized that development of a suitable bioactive scaffold, loaded with NT-3-overexpressing OPCs (OPC-NT-3) and capable of guiding directional axonal regeneration and myelination, could be an important advance in production of white matter-like tissue (WMLT) for SCI repair.

To date, several biomaterials, such as poly (lactic-*co*-glycolic acid), polyethylene glycol, collagen sponge (CS), and chitosan, have been used for SCI repair [4,15,17,18]. These materials exhibit good biocompatibility and can be used to load cells and promote nerve regeneration. A biomaterial scaffold featuring straight channels to guide directional axon regeneration can be produced by 3-dimensional (3D) printing [1]. However, few 3D-printed bio-scaffolds are capable of simulating the micro-topological structure of the ecological niche of oligodendroglial lineage (OL) cells associated with spinal white matter tissue, which are necessary for directional axon regeneration, remyelination and branching [19].

The optic nerve (ON) is derived from central nervous system (CNS) tissue, and decellularized ON (DON) retains the architectural, chemical, and biological information associated with its extracellular matrix (ECM), greatly facilitating its use for repair of injuries to the CNS. However, few studies have evaluated whether DON can enhance CNS repair. Our previous studies suggested that DON microstructure is similar to that of spinal cord white matter, with an ECM similar to that of embryonic optic nerve [20,21].

In this study, we investigated whether DON contains the bioactive components necessary to generate a niche capable of supporting OPC-NT-3 differentiation and maturation that can support construction of a niche-specific WMLT. We expected that a niche-specific WMLT would be able to promote directional axon regeneration and myelination and facilitate functional spinal cord repair.

Abbreviations

SCI	spinal cord injury
WMLT	white matter-like tissue
DON	decellularized optic nerve
NT-3	neurotrophin-3
OPCs	oligodendrocyte precursor cells
OL	oligodendroglial lineage
GDNF	glial cell-derived neurotrophic factor
CNTF	ciliary neurotrophic factor
CST	corticospinal tract
OPC-NT-3	NT-3-overexpressing OPCs
CS	collagen sponge
ON	optic nerve
SN	sciatic nerve
ECM	extracellular matrix
EON	embryonic optic nerve
MON	mature optic nerve
HE	hematoxylin-eosin
CSPGs	chondroitin sulfate proteoglycans
LN	laminin
NSCs	neural stem cells
SCs	Schwann cells
PI	propidium iodide
Hoe	Hoechst33342
CCK8	Cell Counting Kit-8
DRG	dorsal root ganglion
NF	neurofilament
TEM	transmission electron microscopy
GFAP	glial fibrillary acidic protein
IBA-1	Ionized calcium binding adapter molecule 1
SEM	scanning electron microscopy
LAMC1	laminin subunit gamma 1
LAMB2	laminin subunit beta 2
pre-LAMA/C	pre-laminin alpha/gamma
ITGA	integrin alpha
ITGβ	integrin beta
CNS	central nervous system
OPCs	oligodendrocyte precursor cells
COP	committed oligodendrocyte precursor
NFOL	Newly-formed oligodendrocyte
MFOL	Myelin-forming oligodendrocyte
Snap25 + OL	$Snap25^{+}$ oligodendrocyte
Ryr2+OL,	$Ryr2^{+}$ oligodendrocyte
AAV	adeno-associated viral
VGluT	vesicular glutamine transporter
NG2	Neuron-glia antigen 2
LFQ	label-free quantification
UMAP	uniform manifold approximation and projection

2. Materials and methods

2.1. Ethics statement

All animal experiments were conducted in accordance with Sun Yat-sen University guidelines for animal research and use.

2.2. Scaffold preparation and characterization of microstructure

Preparation of decellularized nerve scaffolds was described in our previous study [20]. Briefly, fresh ON and sciatic nerve (SN) were separated from adult pigs (~2 years of age, supplied by Northwest Agriculture and Forestry University, China). The cellular contents of two nerves were sequentially extracted by washing with 3% Triton X-100 (Amresco, Solon, OH, USA), 4% sodium deoxycholate (Sigma-Aldrich, St. Louis, MO, USA), 50 U/ml DNase (Sigma-Aldrich), and 10 μg/ml RNase (Sigma-Aldrich) on a shaker (Allsheng OS-100, Hangzhou, China). The SN was also defatted. The porcine DON and decellularized sciatic nerve (DSN) scaffolds were then freeze-dried for 24 h and stored at 4 °C for up to 1 month until use. All processes were performed under sterile conditions. Commercial CS (BIOT Biology, Wuxi, China) was used as a scaffold for comparison as described below. All procedures involving animals were conducted in accordance with the ethical

standards of the Animal Care and Use Committee of Sun Yat-sen University and the National Institutes of Health Guide for the Care and Use of Laboratory Animals (Institutional Animal Care and Use Committee, Sun Yat-Sen University, Feb 28, 2019, SYSU-IACUC-2019-B034). Hematoxylin-eosin (HE) staining and scanning electron microscopy (SEM) were used to assess transverse and longitudinal scaffold structures. Quantitative analysis of the total number of channels in transverse sections and number of straight channels in longitudinal sections per square millimeter was conducted on 15 scaffolds stained with HE for characterization of microstructure. Channel diameter was assessed from SEM images of five scaffolds (20 channels per scaffold in transverse sections).

2.3. Assessment of ECM proteins on the surfaces of scaffolds

Longitudinal cryosections of the scaffolds (25-μm thickness, $n = 5$ for each group) were cut and mounted on gelatin-coated slides for immunofluorescence staining. After staining for chondroitin sulfate proteoglycans (CSPGs) and laminin (LN), images were captured from the four corners of random fields of each section under a fluorescence microscope (DM6B, Leica, Germany) at a typical magnification of 100 ×. The relative immunofluorescence intensity was determined using ImageJ software (National Institutes of Health, USA).

2.4. Assessment of the viability of neural stem cell-derived cells

Each scaffold was shaped into a short column (3 mm in diameter and 2 mm in length). Neural stem cells (NSCs) were isolated from Sprague-Dawley (SD) rats ($n = 18$, Experimental Animal Center of Sun Yat-sen University, SYSU-IACUC-2019-B034, Guangzhou, China), as described previously [22]. Briefly, rats at postnatal day 1 (P1) were anesthetized and the hippocampus was mechanically dissected and dissociated into a single-cell suspension. The cells were cultured in Dulbecco's modified Eagle's medium (DMEM)/F12 (Hyclone, Logan, UT, USA) containing 1% B27 (Life Technologies, Carlsbad, CA, USA) and 20 ng/ml basic fibroblast growth factor (bFGF, Life Technologies). After 7 days, the cells grew as neurospheres in suspension. Neuroepithelial stem cell protein (Nestin) immunoreactivity was assessed and confirmed for all neurospheres. A total of 2×10^5 NSCs in 20 μl culture medium was seeded onto each scaffold ($n = 5$ in each group). The cell-scaffold mixture was maintained in DMEM/F12 (1:1) supplemented with 1% B27 and 2% fetal bovine serum (FBS, Gibco) for another 5 days.

Cell viability was assessed by propidium iodide/Hoechst33342 (PI/Hoe) staining, for which the NSC-seeded scaffolds were incubated with PI dye solution (500 nM) for 10 min at 5% CO_2 and 37 °C. Then each scaffold was rinsed thoroughly with 0.01 M phosphate buffered saline (PBS), and fixed with 4% paraformaldehyde. These scaffolds were then rinsed and transferred to another well with Hoe dye solution (1 μg/ml) for 10 min. The number of Hoe positive cells indicated the total number of cells, whereas the number of PI positive cells indicated the number of dead cells; the PI/Hoe ratio was used as a measure of cell death. After 5 days in culture, a Cell Counting Kit-8 (CCK-8, Saint-Bio, Shanghai, China) assay was performed on the NSC-seeded scaffolds for 4 h in an atmosphere of 5% CO_2 at 37 °C according to the manufacturer's instructions. Culture plates were shaken for 20 min to allow complete dye dissolution, and then the solution from each scaffold was transferred to another well and this process was repeated three more times. Cell viability was assessed using an absorbance reader (Sunrise, Tecan, Männedorf, Switzerland) at an optical density of 450 nm.

2.5. Dorsal root ganglion neurite outgrowth onto scaffold slices

DON, DSN, and CS scaffolds were cut into 200 μm-thick slices (3 mm in width and 4 mm in length, $n = 5$ for each group). Dorsal root gangli (DRG) with dorsal roots were dissected from P1 GFP transgenic SD rats (Osaka University, Osaka, Japan) and collected in cold DMEM/F12 medium, and then redundant dorsal roots were removed under a stereomicroscope. Two DRGs were placed on every slice, and cultured in DMEM/F12 medium containing 2% B27, 2% FBS, 0.3% L-glutamine, and 100 ng/ml nerve growth factor (NGF, Life Technologies) in a 37 °C incubator with 5% CO_2. The medium was changed every day. After 3 days of culture, the DRGs were fixed with 4% paraformaldehyde in 0.01 M PBS. To assess DRG neurite outgrowth, we measured the length of neurofilament (NF)-positive (NF^+) neurite outgrowth, and used a microscope to manually quantify the percentage of straight-growing NF^+ neurites at an angle of 0°–30° to the longitudinal axis of the scaffold slice. To assess the myelination potential of the three types of scaffold, we observed the number of myelin basic protein (MBP)-positive (MBP^+) Schwann cells (SCs) attached to NF^+ neurites and quantified them under a fluorescence microscope. After 14 days in culture, the DRGs were fixed for observation of the myelin ultrastructure using transmission electron microscopy (TEM, Philips CM 10, Amsterdam, Netherlands).

2.6. Proteomics analysis

The protocol for proteomic analysis was described in detail in our previous study [20]. Briefly, peptide samples from mature optic nerve (MON), embryonic optic nerve (EON), and DON were dissolved in 2% acetonitrile/0.1% formic acid and analyzed using a TripleTOF 5600+ mass spectrometer (Sciex, USA) coupled with an Eksigent nanoLC System (Sciex, USA). The original LC-MS/MS (liquid chromatography tandem mass spectrometry) file data were submitted to ProteinPilot Software v4.5 (Sciex, USA) for data analysis following information-dependent data acquisition. The paragon algorithm of ProteinPilot was used to search the uniprot_sus database (https://www.uniprot.org). Skyline v3.6 software (Sciex, USA) was used for peptide and protein quantification. For determination of differentially expressed proteins, fold-change was calculated as the average of paired comparisons among biological replicates. Proteins with a fold-change > 1.5 and $P < 0.05$ were considered significantly differentially expressed. Each protein was retrieved from the UniProt library and images were generated using R (http://www.r-project.org). The pheatmap function from the pheatmap package was used to perform cluster analysis on the samples according to rows and columns, and a hierarchical clustering heatmap was obtained. Protein interaction networks were identified using the STRING database (https://string-db.org/).

2.7. Quality filtering and analysis of a single cell atlas

To identify the receptor to which LN binds to initiate robust OL cell differentiation and maturation, a single cell atlas was generated employing data from the mouse CNS [23]. Basic quality filtering was performed according to previously described methods [23]. Doublets were detected and removed using the Python package "scrublet" (version 0.2) [24]. In total, 4996 cells were selected for further analysis. The batch effect was eliminated using the Python package "bbknn" [25]. Dimension reduction was performed using the uniform manifold approximation and projection (UMAP) algorithm and clusters were identified using the Louvain clustering algorithm with the default settings from the Python package "Scanpy" (version 1.4.4) [26]. Trajectory inference and Pseudotime analysis were performed according to the pipeline described in a web interface at http://linnarssonlab.org/oligodendrocytes/.

2.8. DON-derived WMLT preparation

NSCs were isolated from green fluorescent protein (GFP) transgenic SD rats. OPCs were obtained according to previous protocols [10]. Briefly, NSCs at passage 2 (Nestin-positive cells) were cultured with DMEM/F12 containing 10 ng/ml platelet-derived growth factor AA (PDGF-AA, Life Technologies), 10 ng/ml bFGF (Life Technologies), 30 ng/ml triiodothyronine (T3, Sigma-Aldrich), and 1% FBS for 3 days. The

cells were transferred when they reached 90% confluency and were purified by differential digestion/adhesion technique. The cells were tested for the expression of neuron-glia antigen 2 (NG2) (EMD Millipore). The purity of the OPCs used in all subsequent experiments was approximately 80% NG2 positive. The OPCs were then transfected with an adeno-associated viral (AAV) vector carrying the NT-3 coding sequence (NM_002527, Vigene Biosciences, Rockville, MD, USA) for 12 h. The scaffolds were manually shaped to the appropriate dimension (1 mm width × 1 mm height × 2 mm length) using a blade. A total of 1×10^5 OPC-NT-3 in 10 μl culture medium was seeded into every scaffold to construct the DON-derived WMLT. The scaffolds were incubated for 3 days. WMLT was tested for expression of NG2, MBP, glial fibrillary acidic protein (GFAP), oligodendrocyte transcription factor 2 (Olig2, a marker for OPCs) and NT-3.

2.9. Spinal cord surgery and transplantation

Adult female SD rats (200–250 g, supplied by the Experimental Animal Center of Sun Yat-sen University, SYSU-IACUC-2019-B034) were randomly divided into six groups ($n = 8$ in each group): 1.) Dorsal white matter injury with no implant (the D-SCI group); 2.) DON scaffold implant (the DON group); 3.) DON scaffold containing OPC implant (the DON-OPC group); 4.) DON scaffold containing OPC-NT-3 (the WMLT group); 5.) CS scaffold containing OPC-NT-3 (the CS-OPC-N group); 6.) normal rats (the Nor group). There were 48 rats in total. Three days before surgery, they were given cyclosporine A (Novartis Pharma Schweiz AG, Eberbach, Germany) by subcutaneous injection (1 mg/100 g per rat). They were anesthetized with 1% pentobarbital sodium (40 mg/kg). A laminectomy was performed at the T9 vertebral level to expose the T10 spinal segment, and the dura was vertically cut with microdissection scissors. Bilateral incisions were made 0.5 mm from the dorsal midline of the spinal cord to form a rectangular gap (1 mm in width, 1 mm in depth, and 2 mm in length) in the T10 segment. Then, different grafts of the same size were used to fill the gaps in corresponding groups. All rats received extensive post-surgery care including intramuscular injection of penicillin (5×10^4 U/kg per day) for 5 days, and manual voiding was performed twice per day until automatic micturition function was reestablished. The cyclosporine A was administrated once a day for 1 month.

2.10. Assessment of locomotor performance

To assess limb coordination and body weight support, the rats ($n = 5$ in the six groups) were assessed 1 month after surgery using footprint analysis according to published protocols with slight modifications [27,28]. The hind-paws of the rats were painted red. While the rats walked on a straight runway (1 m length and 7 cm width), their footprints were recorded on white paper, with each rat walking three times. Within a 50 cm length of white paper, the number of footprints (plantar paw placing with center pad and third toe) in each rat was recorded three times. Sensorimotor impairment was reflected by errors when a rat crossed a horizontal ladder [29]. The 1 m long horizontal ladder walk test equipment consisted of unevenly spaced metal rungs (to prevent habituation) elevated approximately 15 cm from the ground. The rats in six groups ($n = 5$) were pre-trained on the horizontal ladder for 1 week prior to injury. After dorsal white matter injury, rats were tested weekly for up to 4 weeks. The average number of hind limb misplacements while the rat walked along the 1-m-long horizontal ladder three times was manually recorded. A complete miss, slip, or replacement of the paw during placement was considered to be an error. Three independent investigators who were unaware of the treatment received by each rat recorded the data.

2.11. Perfusion and immunofluorescence staining

All rats were deeply anesthetized with 1% pentobarbital sodium (50 mg/kg, intraperitoneally) and intracardially perfused with physiological saline containing 0.002% $NaNO_2$ and 0.002% heparin, followed by 4% paraformaldehyde. After perfusion, the spinal cord was dissected, postfixed overnight in the same fixative, and dehydrated in 30% sucrose. Longitudinal and transverse sections of the selected spinal cord segments were cut to 25-μm thickness using a cryostat and all sections were stored at −30 °C for further processing. For immunofluorescence staining, the sections were rinsed with 0.01 M PBS, blocked with 10% goat serum for 30 min at 37 °C, and incubated with primary antibodies in 0.3% Triton X100 overnight at 4 °C. After rinsing with 0.01 M PBS, the sections were incubated with secondary antibodies for 1 h at 37 °C, and Hoe fluorescence was examined by fluorescence microscopy (DM6B, Leica). A summary of the antibodies used is provided in Table S1.

2.12. Morphological quantification in vivo

We conducted staining for mouse antibody-NF, rabbit anti-vesicular glutamine transporter (VGluT) and rabbit anti-calcitonin gene related peptide (CGRP) to identify regenerated nerve fibers and to quantify straight-growing neurites under the microscope. Chicken anti-MBP antibody staining was performed to identify the myelin sheath. Rabbit anti-CSPG and mouse anti-GFAP antibody staining was performed to assess glial scars. Mouse anti-ionized calcium binding adaptor molecule 1 (IBA-1) antibody staining was performed to identify inflammatory responses. Rabbit anti-LN, chicken anti-NF and mouse anti-integrin alpha (ITGA) antibody staining was performed to assess the mechanism of nerve fiber regeneration. Stained sagittal sections ($n = 5$ in each group) were further analyzed with iMaris (Oxford Instruments, Oxford, UK) and ImageJ software. The relative intensity of NF-, VGluT-, CGRP-, MBP-, LN-, NT-3-, CSPG-, GFAP- and IBA-1-positive areas was measured in selected areas (2 mm length × 1 mm height) within the injury/graft site in each longitudinal section (serial sagittal sections, one in every four sections was used, and six sections were taken from each rat) and used for comparisons. Straight-growing axons within the injury/graft site defined as NF^+ nerve fibers at an angle of 0°–30° to the longitudinal axis of the spinal cord were counted and compared among the WMLT, CS-OPC-N and Nor groups.

2.13. Remyelination ultrastructure

The samples used for ultrastructural observations were post-fixed overnight in a fixative solution containing 2.5% glutaraldehyde and 4% paraformaldehyde at 4 °C. The samples were washed in PBS, and then dehydrated in graded ethanol and flat-embedded in Epon812 (TED PELLA). For *in vivo* quantification, semi-thin sections of spinal cord segment were cut with a Leica RM2065 microtome, stained with toluidine blue (5% in a borax solution), and mounted on glass slides. Five semi-thin sections were selected from the injury/graft site of the spinal cord of each rat for remyelination analysis ($n = 3$ in each group). Three regions of interest were selected in each section and examined at 1000 × magnification. Newborn myelin sheaths (thin sheaths that were light in color) were counted and compared between the WMLT and CS-OPC-N groups. Ultrathin sections (100-nm thickness) of the *in vitro* DRG cultures and the *in vivo* injury/graft site of the spinal cord were cut, double stained with lead citrate and uranyl acetate, and examined by TEM.

2.14. Statistical analysis

Data were analyzed using one-way analysis of variance (ANOVA) and SPSS 20.0 software (International Business Machines Corporation, Armonk, NY, USA). If equal variances were found, the least-significant difference (LSD) test was applied. If variances were not equal, the Kruskal–Wallis test and Dunnett's T3 were applied. Student's *t*-test was used to compare two groups. $P < 0.05$ was considered statistically significant. Simple linear regression was used to analyze the correlation of

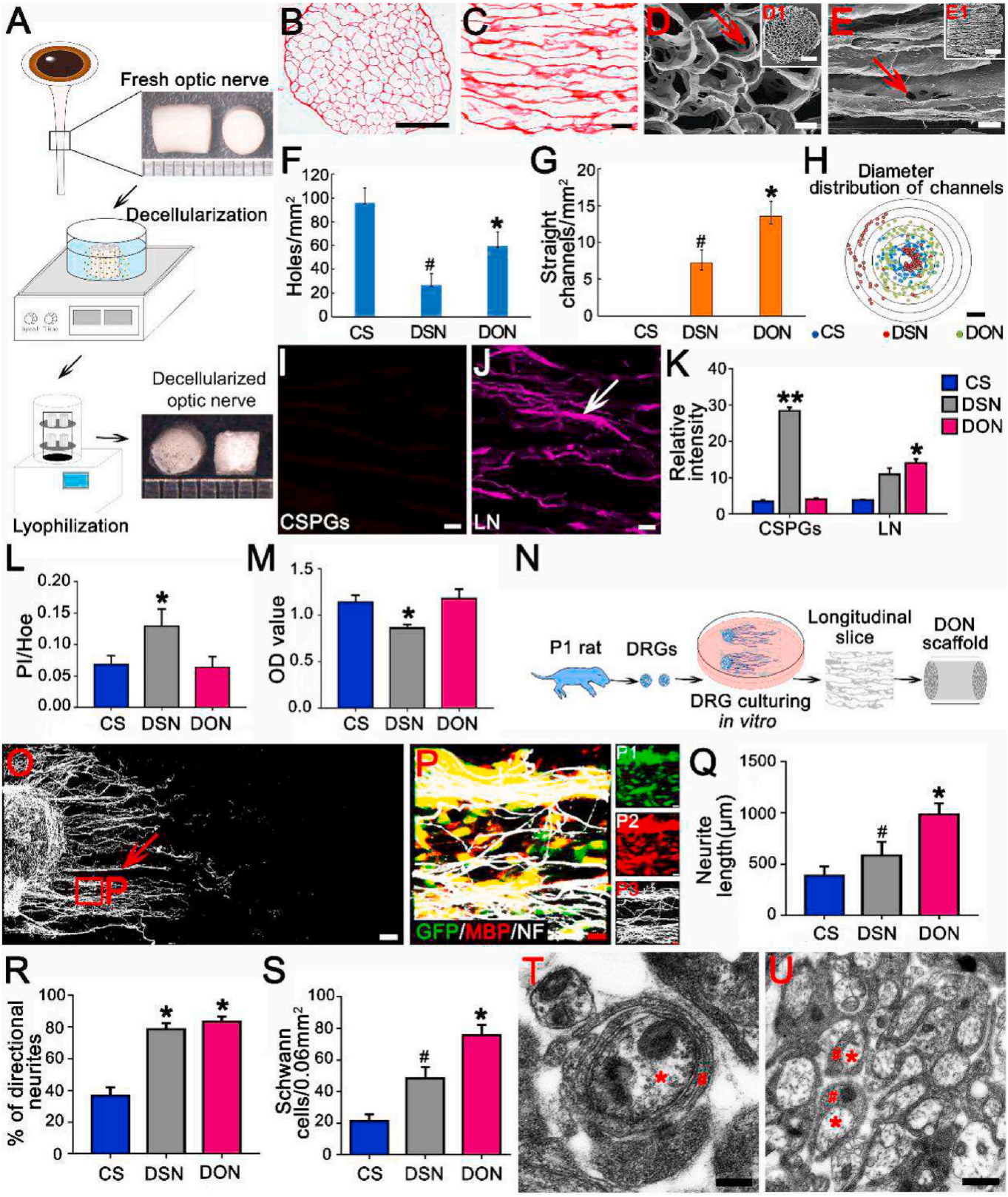

(caption on next page)

Fig. 1. Preparation and characteristics of the DON scaffold. (**A**) A schematic diagram summarizing the decellularization process: fresh porcine ON tissue was subjected to decellularization by chemical extraction and lyophilization. DON scaffolds with an approximate diameter of 3 mm are shown on the right. (**B**)–(**E**) HE staining and scanning electron microscopy (SEM) show structures in transverse (B, D, D1) and longitudinal (C, E, E1) sections of a DON scaffold; no residual nuclei were present. The DON scaffold contained pores in the wall of the channel (20–30 μm, arrows in D and E). (**F**)–(**G**) Bar charts comparing the total number of channels (F, transverse section) and number of straight channels (G, longitudinal section) (* and # indicate $P < 0.01$ when CS was compared with DON or DSN scaffolds, respectively). (**H**) Radar chart showing the distribution of channel diameters. (**I**)–(**M**) Analysis of the ECM and NSC loading capacity of the three types of scaffold. Distribution of CSPGs (I) and LN (J) in the DON scaffold. LN could be observed in a linear arrangement on the surface of the DON scaffold (arrow in J). (**K**) Fluorescence intensity histograms of CSPGs and LN in the CS, DSN, and DON scaffolds (* indicates statistical significance between the DON and CS or DSN scaffolds, *$P < 0.05$, **$P < 0.01$). (**L**)–(**M**) Histogram showing the effects of CS, DSN, and DON scaffolds on the survival and viability of NSC-derived neural cells by PI/Hoe (L) and CCK-8 (M) analysis (* indicates statistical significance between the DSN scaffold and other groups, $P < 0.05$). (**N**)–(**U**) Guidance of DRG neurite growth and myelination by CS, DSN and DON scaffolds. (**N**) Schematic diagram of the strategy used to seed DRGs on longitudinal scaffold slices for 3 days. (**O**) NF^+ neurites (white, indicated by arrow) growing on DON longitudinal slices. (**P**) Enlarged images of the areas in the squares in (O). Fluorescence images showing that MBP^+ SCs (red) adhered strongly to NF^+ neurites. (**Q**) Bar chart showing that neurite length was greatest on DON slices, followed by DSN and CS slices. (**R**) Bar chart showing no significant difference in the percentage of straight neurites between the DON and DSN groups. (**S**) Bar chart showing that the number of SCs wrapping NF^+ neurites was greatest on DON slices, followed by DSN and CS slices (* and # indicate $P < 0.05$ when CS was compared with DON or DSN slices, respectively). (**T**) and (**U**) A DON slice imaged by TEM following 14 days of culture with DRGs *in vitro,* the neurites (red asterisks) were perfectly wrapped by SCs (red hashes). Data are presented as mean ± SD ($n = 5$). One-way ANOVA with an LSD-*t* was performed. Scale bars = 1000 μm in (B); 200 μm in (C); 100 μm in (D)–(E); 100 μm in (H); 60 μm in (I)–(J); 100 μm in (O); 15 μm in (P); 200 nm in (T) and 500 nm in (U).

structure repair with functional recovery. All values are expressed as mean ± standard deviation (SD).

3. Results

3.1. Microstructural characteristics of DON, DSN, and CS scaffolds

A schematic diagram summarizing the decellularization process used to obtain DON and DSN scaffolds is shown in Fig. 1A. The microstructural characteristics of the DON, DSN, and CS scaffolds were analyzed. Transverse and longitudinal sections of the scaffolds were evaluated by HE staining. Channels in CS scaffolds were randomly distributed in both longitudinal and transverse sections (Figs. S1A and E). The DSN scaffold featured straight longitudinal channels, but their diameters were not uniform (Figs. S1B and F). In contrast, the DON scaffold contained evenly distributed straight channels with uniform diameters (Fig. 1B and C). We characterized the topography of each type of scaffold using SEM. In the CS scaffold, channels in both longitudinal and transverse sections were randomly distributed and disordered (Figs. S1C and G). In the DSN scaffold, channel structure was relatively non-uniform (Figs. S1D and H). In contrast, channels in the DON scaffold were evenly distributed and connected by pore structures (20–30 μm; Fig. 1D and E). Analysis of the channels in each scaffold showed that the CS scaffold contained the largest number of channels, but they were not straight, whereas the DSN scaffold had the smallest number and they were straighter. Importantly, the DON scaffold featured the largest number of straight channels, which could help guide axon regeneration (Fig. 1F and G). Both the DON and CS scaffolds featured channel diameters between 100 and 200 μm, but the channel diameters in the DSN scaffold were either smaller than 50 μm or larger than 400 μm, which may not provide adequate surface area for cell adhesion (Fig. 1H).

3.2. ECM proteins on scaffold surfaces

Two major ECM proteins associated with neurite growth were examined by immunofluorescence staining: CSPGs, which inhibit neurite growth, and LN, which promotes neurite growth. CSPGs were rarely detected in the DON and CS scaffolds, whereas the DSN scaffold frequently contained CSPGs. The DON scaffold contained the highest levels of LN, followed by the DSN and CS scaffolds ($n = 5$ in each group, $P < 0.05$; Fig. 1I–K and Fig. S1I–L). These results indicated that the DON scaffold contains abundant levels of LN, which could promote neurite growth, and low levels of CSPGs that inhibit neurite growth. The CS scaffold did not contain LN or CSPGs, suggesting that it is likely to show no obvious tendency for regulating axonal growth.

3.3. Neural stem cell viability and growth on scaffolds

Before neurospheres were seeded onto scaffolds, Nestin immunoreactivity was confirmed. The viability of NSC-derived cells seeded onto each scaffold was examined after 5 days in culture. PI/Hoe staining ($n = 5$ in each group, $P < 0.05$; Fig. 1L and Fig. S2) and CCK-8 analyses ($n = 5$ in each group, $P < 0.05$; Fig. 1M) showed that NSC-derived cells displayed improved growth and viability when grown on the DON and CS scaffolds as compared with the DSN scaffold.

3.4. Directional outgrowth of dorsal root ganglion neurites in vitro

Next, the ability of each scaffold to support neurite extension was examined using a DRG culture model (Fig. 1N). Freshly isolated DRG cells were seeded onto DON slices in the wells of a culture plate and grown for 3 days. DSN and CS slices were used as controls. The cultures were analyzed for NF immunofluorescence, and the maximum lengths of DRG neurite extensions were measured. All slices supported robust NF^+ neurite extension, with the longest neurites occurring on the DON slices, followed by those grown on the DSN and CS slices. Analysis of oriented NF^+ neurites growing at angles ranging from 0° to 30° relative to the longitudinal slice axis revealed that the DON and DSN slices supported optimal, directional neurite growth ($n = 5$ in each group, $P < 0.05$; Fig. 1O–R and Fig. S3). These results indicated that the DON scaffold was the most conducive for directional growth of DRG neurites.

3.5. Myelination of DRG neurites

The potential of each scaffold to support myelination was evaluated using the DRG culture system. To distinguish between DRG neurites and SCs, the cultures were stained for NF and MBP. More MBP^+ SCs adhered to NF^+ neurites in the DON scaffold than in the DSN or CS scaffolds ($n = 5$ in each group, $P < 0.05$; Fig. 1P, S and Fig. S3). Next, myelination potential of the SCs was investigated using TEM. After culturing for 2 weeks, SCs were observed on the DON scaffold at various stages of myelination, including a multilayer myelin sheath structure and early myelinated neurites (Fig. 1T, U). These results suggested that the DON scaffold may be better able than the DSN and CS scaffolds to promote SC-mediated myelination of DRG neurites. Combined with results indicating spinal cord histocompatibility (Fig. S4 shows fewer $GFAP^+$ and $IBA\text{-}1^+$ cells in the engrafted DON scaffold than in the engrafted CS scaffold at the injury/graft sites of spinal cords), these results demonstrate the ability of DON scaffolds to direct axonal regeneration and myelination for use in construction of WMLT.

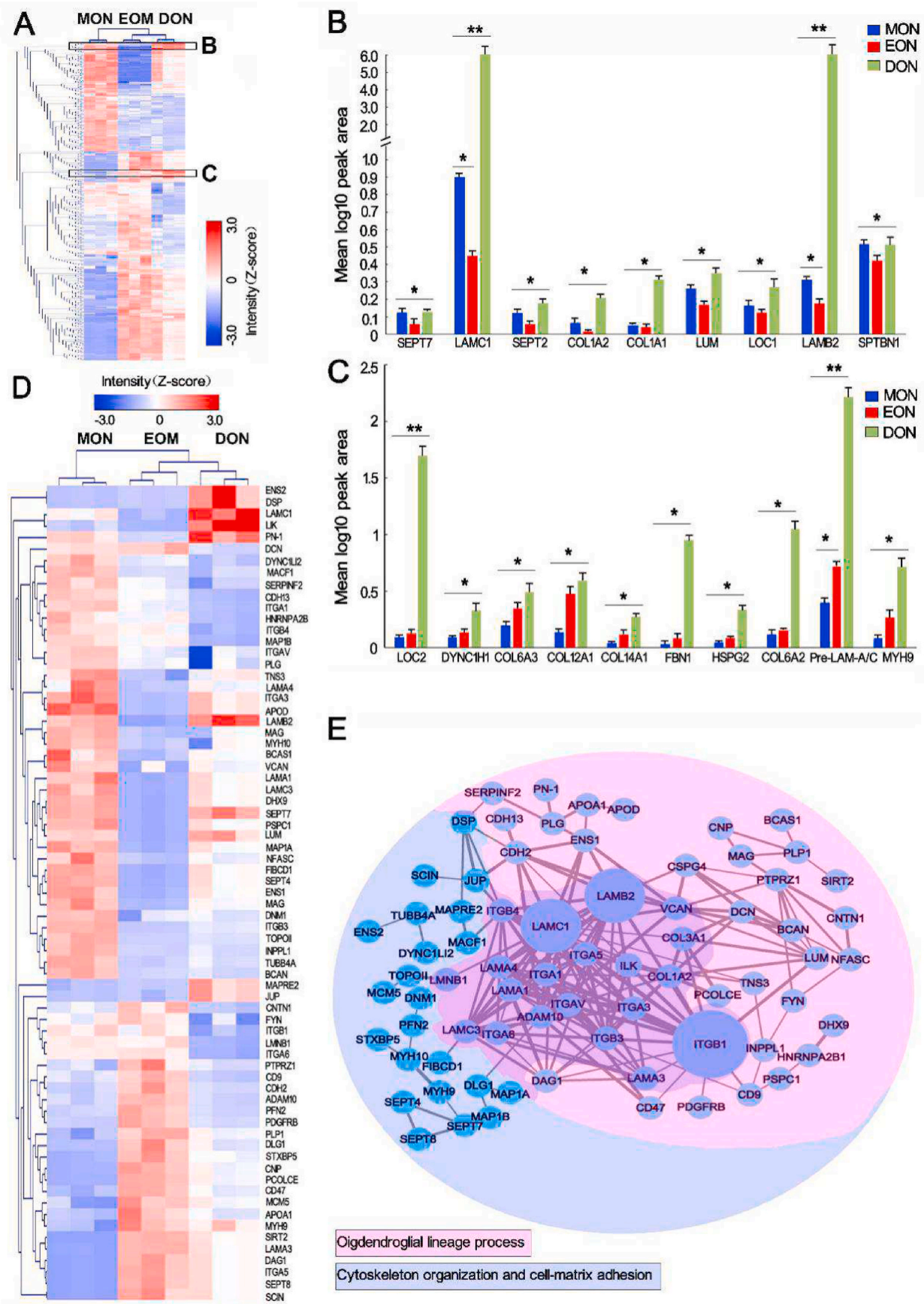

(caption on next page)

Fig. 2. Quantitative proteomics analysis of MON, EON and DON. (**A**) Heatmap representation of proteins that are expressed at significantly different levels ($P < 0.05$) across the three groups. Z-scored label-free quantification (LFQ) intensities are depicted; red and blue represent increased and decreased values, respectively. (**B**) and (**C**) Region of interest (black box in A) containing proteins associated with OL cell maturation (B) and OPC differentiation (C) that were tested for expression. The results were significant across every group, with data input as values to the base 10 to allow for log adjustment ($n = 3$, $^{**}P < 0.0001$, $^{*}P < 0.001$). (**D**) and (**E**) Heatmap and protein–protein interaction network constructed from 71 significantly differentially expressed proteins related to lineage development, cytoskeletal organization, and cell-matrix adhesion of OL cells. Z-scored LFQ intensities (D) for which red and blue represent increased and decreased values, respectively. Protein–protein interaction network analysis (E) by strings (confidence cutoff: 0.7). The thickness of the line represents the direct correlation strength of the two proteins, and the size of the nodes (circles) represents the magnitude of the protein effect (networks are based on the string database, https://string-db.org/). The proteins are sorted by color into the two different categories.

3.6. Protein components in DON forming an ecological niche for OL cell development

To determine whether DON could be loaded with OPC-NT-3 to construct WMLT, the ECM protein components of the DON were analyzed using proteomics analysis. The results showed that DON contained 1179 protein types, while 2336 and 3318 proteins were detected in MON and EON, respectively. According to a hierarchical clustering heatmap (Fig. 2A), when compared with MON, DON retained more proteins that could promote colonization and myelination of OL cells, with laminin subunit gamma 1 (LAMC1) and laminin subunit beta 2 (LAMB2) being the most abundant (Fig. 2B). Moreover, DON contained protein components similar to those in EON that can promote terminal differentiation of OPCs, among which the pre-laminin alpha/gamma (pre-LAMA/C) subunits were the most abundant (Fig. 2C). The heatmap and protein-protein interaction network indicated that interactions of LN (LAMC1 and LAMB2) with LN receptors (integrin alpha [ITGA] or beta [ITGB] subtypes) or other adhesion molecules on the cell surface not only significantly affected the colonization and migration of OL cells but also influenced their development, differentiation, maturation, and myelination (Fig. 2D and E). The results suggest that LN-based protein components in DON are conducive to forming a niche for OL cell development, and that DON is a particularly suitable scaffold for constructing WMLT.

3.7. Transcription of LN and LN receptor genes during oligodendrocyte lineage progression

To confirm the effects of LN on lineage progression of oligodendrocytes in the CNS, a single cell atlas of LN and the LN receptor genes was constructed. We downloaded single-cell sequence data from ArrayExpress (accession number: E-GEOD-75330) and performed quality filtering as described in the original report [23]. After reclustering the data using the UMAP and Leiden algorithms, we re-annotated the mouse CNS single cell atlas (Fig. 3A). A more comprehensive cell atlas was mapped than in the original report, which revealed the developmental trajectory from OPCs to mature oligodendrocytes. Intriguingly, by marking cell types with known marker genes (*Cspg4*, oligodendrocyte precursor cells; *Neu4*, differentiation-committed oligodendrocyte precursors; *Tmem2*, newly-formed oligodendrocytes 1; *Ctps*, newly-formed oligodendrocytes 2; *Snhg11*, newly-formed oligodendrocytes 3; *Opalin*, myelin-forming oligodendrocytes 1; *Ptgds*, myelin-forming oligodendrocytes 2; *Klk6*, mature oligodendrocytes; and *Snap25*, Snap25^{+} oligodendrocytes; Fig. 3B and C), we found that LN receptor genes (*Rpsa/Itgb1/Agm/Mcam*) were widely expressed in differentiating and mature oligodendrocytes, but rarely in OPCs (Fig. 3D and E).

We also explored the network relationship of LN subtypes and their receptors. The results revealed that several LN subtype genes, including *Lama1*, *Lama2*, *Lama4*, *Lamb1*, *Lamb2*, *Lamc1*, and *Lamc4*, were highly integrated with each other to form LN complexes via binding to their receptors and promoted oligodendrocyte differentiation and maturation (Fig. 3F). The single cell atlas showed that *Lamc1* was continuously transcribed in OPCs throughout lineage maturation, suggesting that OL cells may secrete LAMC1 to build an ecological niche able to promote their own development. The results also showed that OL cells rarely transcribed *Ntf3* (NT-3 gene) throughout lineage development (Fig. S5), but neurotrophic tyrosine kinase receptor type 3 (*Ntrk3*; TrkC gene) was transcribed (Fig. 3D and E), suggesting that OL cells mainly depend on other cell types to synthesize and secrete NT-3 to promote their development.

3.8. Construction of DON-derived WMLT

Nestin-positive NSCs (Fig. 4A) were induced to differentiate into OPCs, which were then transfected with an AAV vector carrying the NT-3 gene to induce them to overexpress NT-3. The resulting OPC-NT-3 were seeded onto a DON scaffold to generate WMLT. After 7 days in culture, the OPC-NT-3 cells tested positive for MBP and NG2 (Fig. 4B–D) and showed high levels of Olig2 and NT-3 expression (Fig. 4E). Approximately 85% of the differentiating cells expressed the oligodendrocyte marker MBP, whereas approximately 15% of cells expressed GFAP at this time point (Fig. 4C). The transfection rate for the AAV-mediated NT-3 gene exceeded 80% in cultured OPC-NT-3 (Fig. 4D). TEM revealed thin myelin laminae in the WMLT, indicating stable loading of modified OPC-NT-3 onto these scaffolds and demonstrating their myelination potential (Fig. 4F). These results encouraged us to attempt WMLT transplantation at the SCI site to verify its effects on white matter injury repair (Fig. 4G). In WMLT, GFP-positive (GFP^{+}) OL cells were evenly distributed along the straight longitudinal channels of DON. The OL cells in adjacent channels could migrate to or connect with each other through the transverse micron-sized pores of DON (Fig. 4H). Immunohistochemistry revealed that ITGA or ITGB expressed on the surface of the GFP $^{+}$ OL cells could strongly adhere to LN that was deposited in the DON channels (Fig. 4I–K).

3.9. Transplantation and behavioral analysis

One month after WMLT was transplanted into the T10 spinal cord of a rat model of dorsal white matter injury, the hind limbs of rats in the WMLT group showed significant improvement in coordinated motor functions and body weight support compared with those in the control groups (D-SCI [dorsal white matter injury with no implant], DON, DON-OPC, and CS-OPC-N [OPC-NT-3 seeded onto CS]; Fig. 5A–C). Footprint analyses revealed that rats from the WMLT group exhibited a higher number of hind footprints (12.60 ± 1.52) than those in the control groups (the D-SCI, DON, DON-OPC, and CS-OPC-N groups; Fig. 5B). The horizontal ladder-walking test (Videos S1–S6 showing walking test) was used to evaluate skilled locomotion, sensorimotor integration, and limb placement 1 month after WMLT was transplanted at the white matter injury site. When traversing the ladder, the rats from the WMLT group showed overall improvements in performance and consistently reduced hind limb errors (1.07 ± 0.80) compared with those of the control groups (the D-SCI, DON, DON-OPC, and CS-OPC-N groups; Fig. 5C and Videos S1–S6 showing the walking test).

3.10. Nerve fiber regeneration

One month after transplantation, both the WMLT and CS-OPC-N groups provided favorable microenvironments that promoted survival of cells seeded onto those scaffolds. However, the grafted OPCs in the lesions were oriented more along the spinal cord longitudinal axis in the WMLT group (Fig. 5D, F) than in the CS-OPC-N group (Fig. 5E, G). In

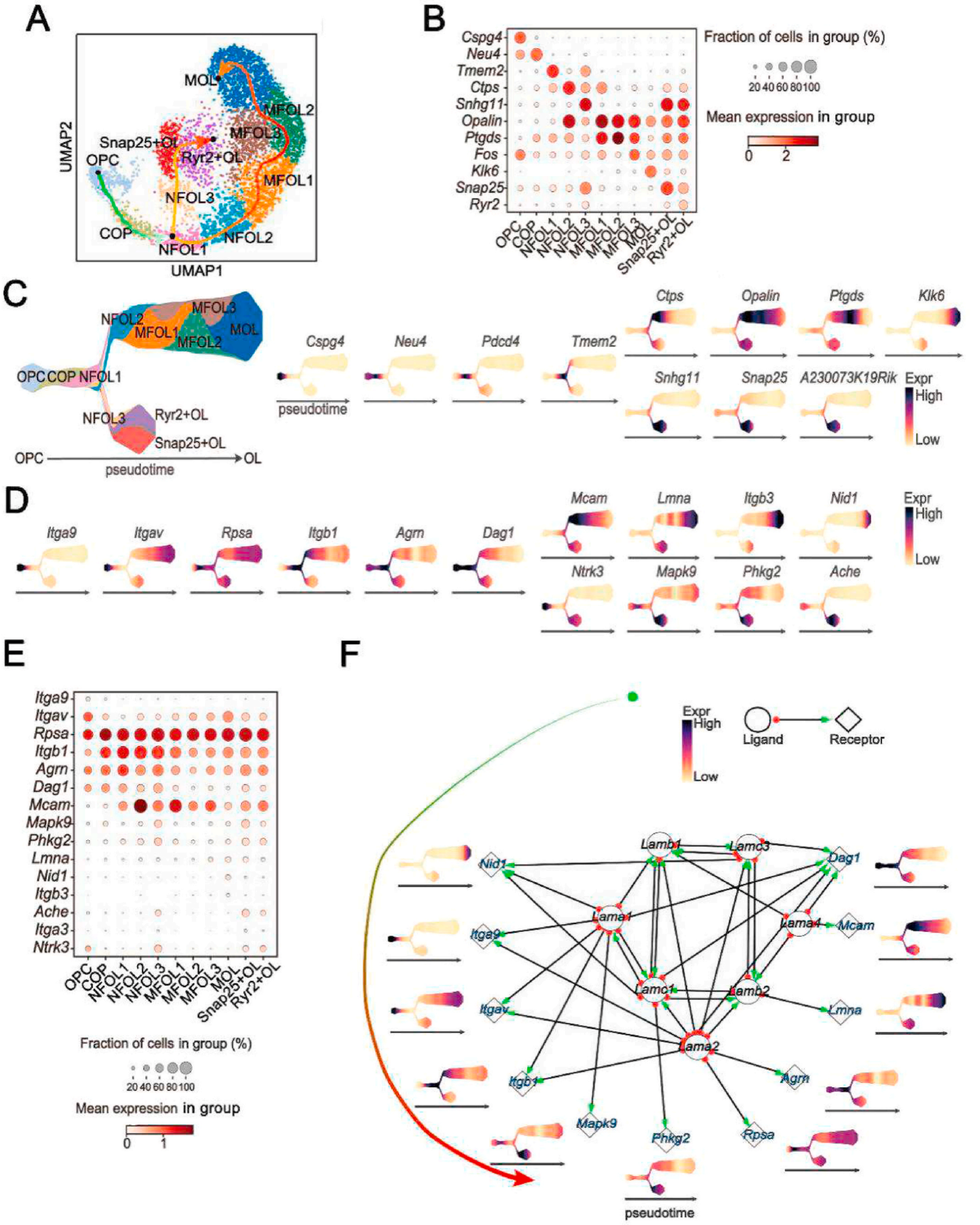

(caption on next page)

Fig. 3. Transcription of LN and LN receptor genes during OL cell development in the CNS. (**A**) UMAP plot showing the cells of the single cell atlas. Cell types are indicated by color. (**B**) Transcription of marker genes in different cell types (OPC, oligodendrocyte precursor cells; COP, committed oligodendrocyte precursors; NFOL, newly-formed oligodendrocytes; MFOL, myelin-forming oligodendrocytes; Snap25 + OL, Snap25$^+$ oligodendrocytes; Ryr2+OL, Ryr2$^+$ oligodendrocytes). (**C**) A Pseudotime axis showing temporal-specific expression of marker genes during differentiation and maturation of OL cells (Cspg4, oligodendrocyte precursor cells; Neu4, differentiation-committed oligodendrocyte precursors; Tmem2, newly-formed oligodendrocytes 1; Ctps, newly-formed oligodendrocytes 2; Snhg11, newly-formed oligodendrocytes 3; Opalin, myelin-forming oligodendrocytes 1; Ptgds, myelin-forming oligodendrocytes 2; Klk6, mature oligodendrocytes; Snap25, Snap25$^+$ oligodendrocytes; Ryr2, Ryr2$^+$ oligodendrocytes). (**D**) and (**E**) Transcription of LN receptor genes during OL cell differentiation and maturation were assessed by analysis of Pseudotime (D) and relative quantity (E). (**F**) Correlation between LN subtype genes and their corresponding receptor genes.

addition, directional regeneration of host NF $^+$ nerve fibers within the lesion was parallel to the longitudinal axis of the spinal cord in the WMLT group (Fig. 5F). In contrast, in the CS-OPC-N group, orientation of the regenerated NF $^+$ nerve fibers in the lesions was more random (Fig. 5G). Quantitative analysis showed significantly larger numbers of oriented NF $^+$ nerve fibers (length greater than 50 μm with a 0°–30° angle between the NF $^+$ nerve fiber and the longitudinal axis of the spinal cord) at the injury site (2 mm length × 1 mm height) in the WMLT group than in the CS-OPC-N group (Fig. 5H and I). Vesicular glutamine transporter-positive (VGluT$^+$) nerve fibers in the WMLT group (Fig. 6A, C) penetrated longitudinally into the transplant region, suggesting re-establishment of descending nerve fibers associated with motor function. In addition, regeneration of sensory nerve fibers in the WMLT group was assessed using CGRP immunoreactivity (Fig. 6E). Both VGluT$^+$ and CGRP-positive (CGRP$^+$) nerve fibers were similarly oriented at the injury/graft site of the WMLT group, whereas the CS-OPC-N group was characterized by disordered regeneration (Fig. 6B, D, F). Quantitative analysis indicated that the region of VGluT$^+$ and CGRP $^+$ nerve fibers at the injury/graft site (2 mm length × 1 mm height) was significantly larger in the WMLT group than in the CS-OPC-N group (Fig. 6G and H). Simple linear regression demonstrated a significant correlation between the NF $^+$ area ratio (Fig. 5I) in the injury/graft site and hind limb errors (Fig. 5C) in the WMLT group (Fig. S6A). These results were consistent with the observed improvements in behavioral functions in the WMLT group.

3.11. Implantation of WMLT enhances axon remyelination

Higher levels of MBP were expressed in the lesions of the WMLT group than in the control groups (the D-SCI, DON, DON-OPC, and CS-OPC-N groups; Fig. 5J). To verify the effects of WMLT implants on axon myelination, the transplanted areas were examined. In the WMLT group, most regenerated nerve fibers at the injury/graft site were wrapped in new myelin sheaths, whereas few nerve fibers were myelinated in the CS-OPC-N group (Fig. 7A–D). Immunofluorescence staining and TEM analyses confirmed that WMLT implants enhanced axon myelination (Fig. 7E–G). Simple linear regression showed a strong correlation between the MBP $^+$ area ratio (Fig. 5J) at the injury/graft site and hind limb errors (Fig. 5C) in the WMLT group (Fig. S6B), which suggests that myelinated axons may play an important role in functional recovery of the hind limbs.

3.12. LN promotion and guidance of directional nerve regeneration

To explore the mechanisms by which implanted WMLT promotes directional nerve regeneration, we examined LN expression 1 month after WMLT transplantation. We found that LN was deposited linearly on the surfaces of DON channels, and that GFP $^+$ cells and NF $^+$ nerve fibers were distributed in a similar pattern in the graft (Fig. 8A and B). Further examination revealed that NT-3 secreted by GFP$^+$ cells could bind tightly to LN (Fig. 8C and D). We also found that LN could induce axonal adhesion and extension via specific interactions with ITGA on the axon surface (Fig. 8E–I). Hexprog (spherical polarity Fourier correlation) software analysis showed strong intermolecular electrostatic and van der Waals forces between LN and NT-3 (Fig. 8J), suggesting that LN can tightly bind NT-3 and slow its release. The CS scaffold does not contain LN, and LN and NT-3 expression in the transplanted region of the CS-OPC-N group was significantly lower than that in the WMLT group (Fig. 8K and Figs. S7A–C). Both LN deposition and NT-3$^+$ cells appeared to be irregularly distributed in the CS-OPC-N group (Figs. S7A–C). These results suggested that LN, which was abundantly and linearly deposited on the DON channel surface, may be important for guiding axonal regeneration. Thus, a local NT-3-rich microenvironment might provide an effective chemotactic signal for TrkC $^+$ nerve fiber growth into the WMLT graft (Figs. S7A–C and Fig. S8), with LN directing the orientation of axons by binding to ITGA on their surface (Fig. 8L).

3.13. WMLT reduces inflammation and scar formation

One month after transplantation, levels of CSPGs, GFAP, and IBA-1 were evaluated in the WMLT and CS-OPC-N groups (Figs. S7D–F and Figs. S9A–C), and it was observed that their expression was less in the graft than in the surrounding regions of the spinal cord in the WMLT group (Figs. S9D–I). In addition, WMLT transplantation decreased CSPG and GFAP expression and resulted in fewer IBA-1$^+$ cells within the injury/graft site compared with the CS-OPC-N group ($P < 0.05$; Figs. S7D–F and Fig. S9J). These results indicated that transplanted WMLT attenuated inflammation and scar formation, and provided a microenvironment that is suitable for nerve fiber regeneration and myelination. Moreover, nerve fiber regeneration at the boundary between the transplant and host tissue confirmed that the WMLT integrated well with host spinal cord tissue (Figs. S10A–D).

4. Discussion

A major challenge to SCI repair is providing a microenvironment that is favorable to directional guidance of axon regeneration and myelination [1,30,31], and addressing this challenge will require the three primary tissue engineering elements: seed cells, bioactive factors, and biomaterials [7,32]. The current study aimed to apply tissue engineering strategies to generation of a spinal cord WMLT capable of efficiently guiding axon regeneration and myelination during SCI repair.

4.1. Advantages of the DON scaffold: micro-topological structure and bioactive ECM niche

Many studies have shown that compared with single-component biomaterials such as collagen, gelatin, and chitosan, decellularized ECM proteins derived from nervous tissue (such as sciatic nerves or the spinal cord) can provide signals that promote axonal regeneration and myelination [20,33,34]. Although decellularized scaffolds derived from spinal cord tissue more closely resemble ECM of the normal spinal cord, their internal channels collapse after decellularization, which does not support seeding of cells or directional guidance of axon regeneration [35,36]. Therefore, we sought an alternative nervous tissue and focused on the use of ON as a source of scaffold material. In this study, the microstructural and ECM characteristics of DON, DSN, and CS scaffolds were evaluated for use in WMLT and SCI repair.

One advantage of the DON scaffold is its micro-topological structure. Our previously established decellularization program effectively removes cells, nucleic acids, myelin, and other components from the ON while retaining the ECM and scaffold structure with low immunogenicity [20]. Both HE staining and SEM revealed uniformly distributed straight channels in the DON scaffold, with diameters between 100 and

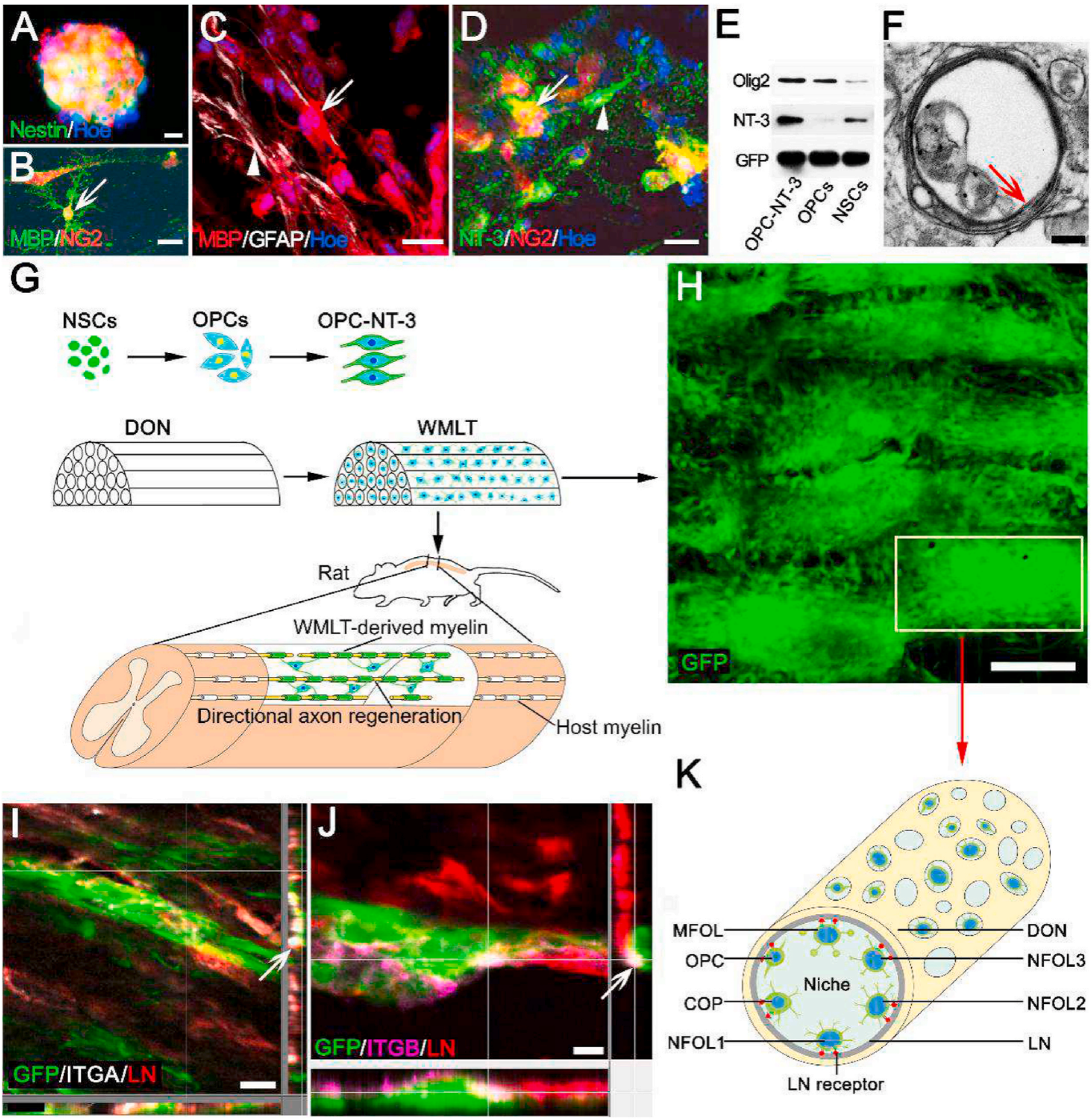

Fig. 4. WMLT construction with integration of gene-modified OPC-NT-3 cells into DON. (**A**) and (**B**) Nestin-positive NSCs (A) were induced to differentiate into MBP/NG2-double positive cells (arrow in B). (**C**) and (**D**) After culturing on the DON scaffold for 7 days, the cells were double-stained for MBP (arrow in C) and GFAP (arrowhead in C), and NT-3 (arrowhead in D) and NG2 (arrow in D). (**E**) Western blot showing Olig2, NT-3 and GFP protein expression in cultured OPC-NT-3/DON, OPCs/DON and NSCs/DON. (**F**) WMLT contained immature myelin sheaths (arrow). (**G**) Schematic diagram of construction and transplantation of WMLT. (**H**) Spatial distribution of WMLT cells. (**I**)–(**K**) LN receptor (ITGA in I, ITGB in J) expressed on GFP $^{+}$ OL cells could strongly adhere to LN on scaffold surfaces (OPCs, oligodendrocyte precursor cells; COP, committed oligodendrocyte precursor; NFOL, newly-formed oligodendrocyte; MFOL, myelin-forming oligodendrocyte). Scale bars = 20 μm in (A)–(D); 200 nm in (F); 150 μm in (H); 20 μm in (I); 10 μm in (J).

200 μm. These channel diameters were similar to those observed in the CS scaffold, suggesting that both scaffolds have similar cell loading capacities. Large numbers of naturally distributed, micron-sized pores were observed in the DON scaffold channel walls, which may provide favorable paths for glial cell migration, axon branching, and cell–cell communication. Future studies can explore the improvements of other biomaterials with the advantages of DON, such as 3D printed CS scaffolds with directional channels and channel surfaces coated with neurotrophic factor-loaded LN. Although 3D printing can produce a variety of biological materials with straight channels, the accuracy of this technique is currently insufficient for introducing micron-sized pores into channel walls. Therefore, 3D-printed scaffolds do not readily allow for the type of cell–cell contact and other information exchange between channels required for rapid cell migration and

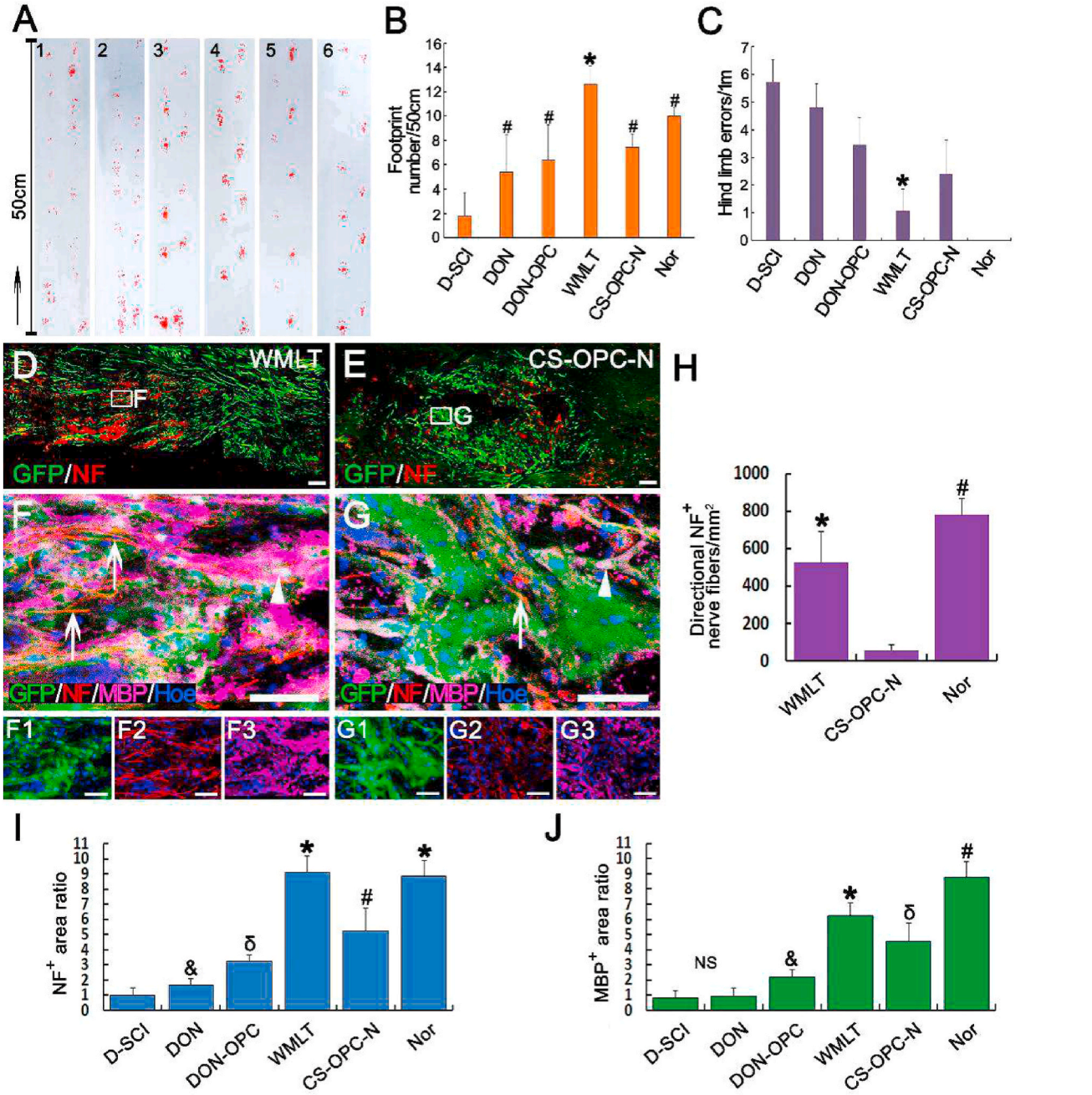

Fig. 5. Rat behavior and directional axon regeneration and myelination in the injured spinal cord after transplantation of WMLT. (**A**)–(**C**) The footprints of both hind limbs (A, B) and horizontal ladder-walking test (C) showed that rats in the WMLT group had improved overall fine motor function (A, groups: 1, D-SCI; 2, DON; 3, DON-OPC; 4, WMLT group; 5, CS-OPC-N; 6, Nor [normal rats]), a significant increase in the footprint number (B, * and # indicate $P < 0.05$ when the D-SCI group was compared with the DON, DON-OPC, WMLT, CS-OPC-N and Nor groups), and a significant decrease in hind limb errors (C, * indicate $P < 0.05$ when the WMLT group was compared with the other groups). Data are presented as mean ± SD ($n = 5$). (**D**) and (**E**) A longitudinal section of spinal cord containing GFP^+ cells and NF^+ nerve fibers in the WMLT (D) and CS-OPC-N (E) groups. (**F**)–(**G3**) NF^+ nerve fibers (arrows) were surrounded by GFP and MBP double-positive cells (arrowheads). (**H**) There were more regenerating NF^+ nerve fibers in the WMLT group aligned with the longitudinal axis of the spinal cord than in the CS-OPC-N group (* and # indicate $P < 0.05$ when the CS-OPC-N group was compared with the WMLT and Nor groups). (**I**) and (**J**) Relative expression levels of NF^+ (I) and MBP^+ (J) in the D-SCI, DON, DON-OPC, WMLT, CS-OPC-N and Nor groups (*, #, δ and &symbols indicate $P < 0.05$ when the D-SCI group was compared with the DON, DON-OPC, WMLT, CS-OPC-N and Nor groups). Data are presented as mean ± SD ($n = 5$). One-way ANOVA with an LSD-*t* test was performed. Scale bars = 200 μm in (D)–(E); 50 μm in (F)–(G3).

diffusion of bioactive substances.

The second advantage of the DON scaffold is that the associated ECM components are derived from the CNS. Our previous research removed various components from the ON of adult pigs, such as myelin-associated glycoprotein and CSPGs, which can inhibit nerve regeneration [20]. The *in vitro* DRG culture results indicated that the direct channels in the DON scaffold and the ECM microenvironment play important roles in guiding direct axonal regeneration and myelination, demonstrating the superiority of the DON scaffold over the DSN and CS scaffolds. However, few studies have examined DON scaffold transplantation *in vivo* or in tissue engineering applications.

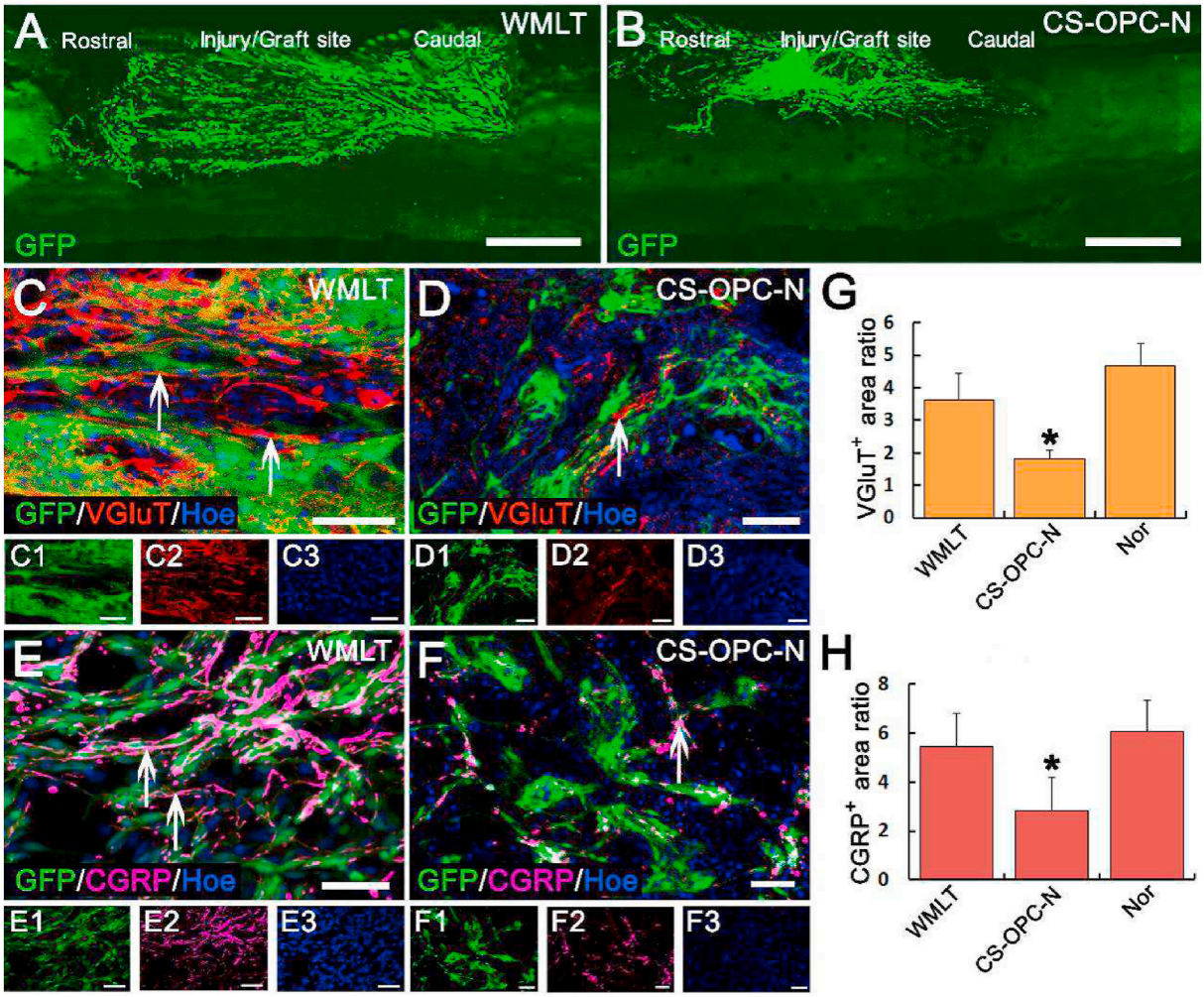

Fig. 6. WMLT guided and promoted regeneration of VGluT- and CGRP-positive nerve fibers. (**A**) and (**B**) Distribution of GFP $^{+}$ OPC-NT-3 after transplantation into the WMLT (A) and CS-OPC-N groups (B). (**C**) and (**D**) VGluT $^{+}$ nerve fibers passed longitudinally through the spinal cord injury/graft site 1 month after transplantation in the WMLT group (arrows in C), while some extended in a disorderly fashion in the CS-OPC-N group (arrow in D). (**E**) and (**F**) CGRP^{+} nerve fibers regenerated in a similar way with VGluT^{+} nerve fibers in the two groups. More CGRP $^{+}$ nerve fibers could be directly regenerated in the WMLT group (arrows in E), while a few CGRP $^{+}$ nerve fibers were regenerated in a disorderly fashion in the CS-OPC-N group (arrow in F). (**G**) and (**H**) Bar chart showing relative fluorescence intensity of the VGluT $^{+}$ area (G) and CGRP^{+} (H) areas at the injury/graft site in the three groups (* indicates statistical significance between the CS-OPC-N and other groups, $P < 0.05$). Data are presented as mean ± SD ($n = 5$). One-way ANOVA with an LSD-*t* test was performed. Scale bars = 1000 μm in (A) and (B); 50 μm in (C)–(F).

4.2. DON niche for OL cells

The ON is part of the CNS, which is an important tissue for lineage progression and terminal differentiation of oligodendrocytes. Our previously published studies suggested that some ECM components of the DON are similar to those of the EON [20]. Further proteomic analysis indicated that the protein components of the DON can create a specific niche able to promote colonization, differentiation, maturation, and myelination of the OL cells. Moreover, the protein–protein interaction network results confirmed that LN is the main component of the DON niche, and can affect migration, colonization, differentiation, maturation, and myelination of OL cells through interaction with LN receptors [23,37]. In addition, the CNS single cell atlas confirmed that OL cells continuously express various LN receptors during maturation. Our results also suggested that OL cells can synthesize and secrete LAMC1 to facilitate colonization during development and maturation. The high levels of LAMC1 expression in DON indicate that it might act as a bioactive material for loading OPCs and constructing WMLT. Furthermore, we observed little *Ntf3* (NT-3 gene) transcription and much *Ntrk3* (TrkC gene) transcription during development of OL cells, which indicates that differentiation and maturation of OL cells depend on exogenous NT-3 [14,38]. These results support our hypothesis that WMLT can be generated by seeding LN-rich DON with OPC-NT-3 to guide directional axon regeneration and myelination. This WMLT contains unique microstructures that form a specific microenvironmental niche favorable to axonal extension and myelination, thus facilitating effective structural and functional integration with the host spinal cord [6,8,10]. The proteomics analysis suggested that there are some proteins other than LN and NT-3 that can promote axon regeneration or myelination, and the mechanisms of these proteins should be explored in future research.

4.3. The important role played by WMLT in repair of SCI

We seeded OPC-NT-3 onto DON (WMLT group) and CS (CS-OPC-N group) scaffolds to construct tissue-engineered nerve scaffolds capable of continuously secreting NT-3 and myelinating regenerating axons. A rat model with a white matter defect in the dorsal spinal cord of the T10 segment was used, which results in the loss of CST control of hind limb motor neurons and damages the ascending pathway that delivers

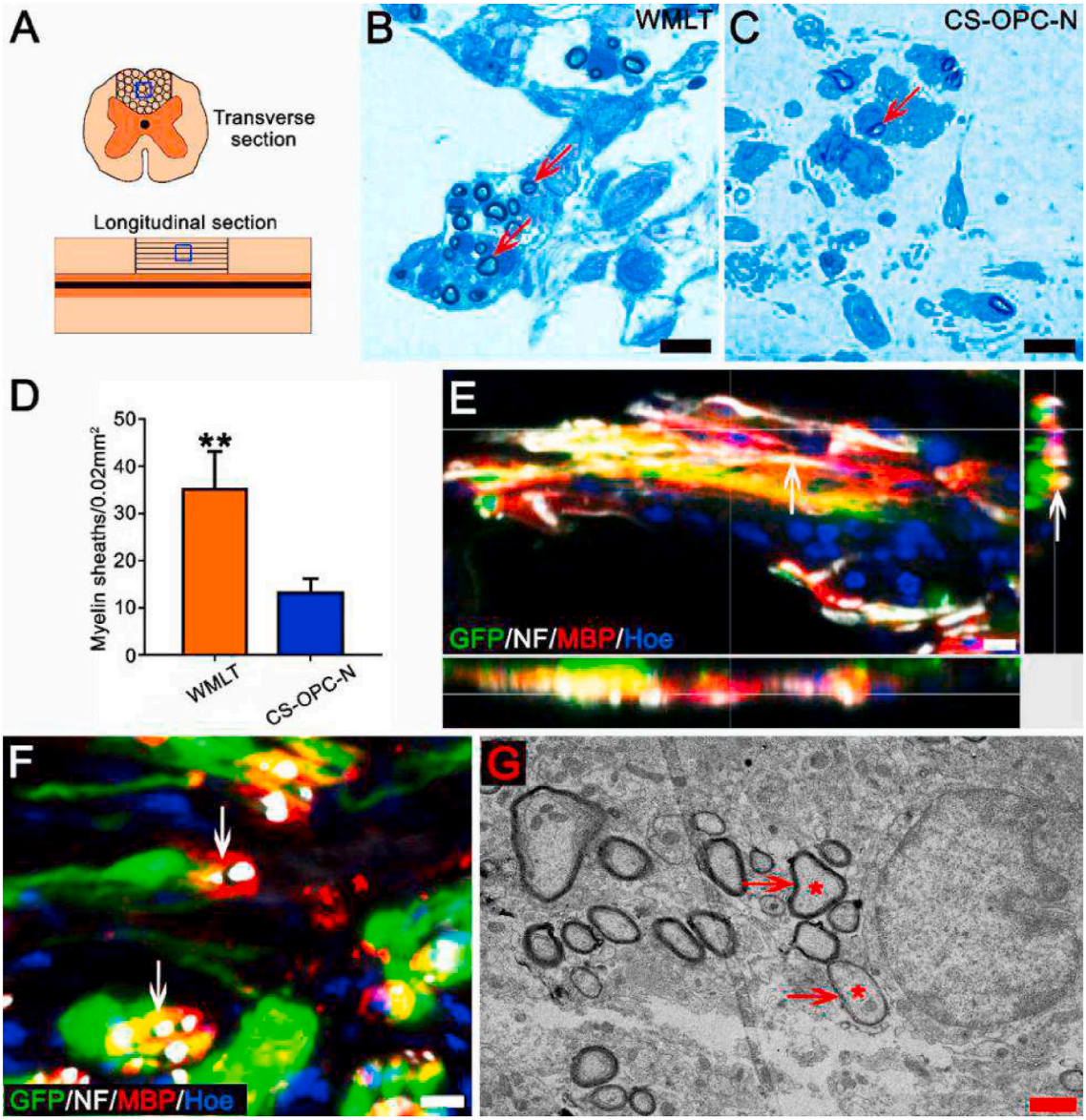

Fig. 7. Impact of WMLT on myelin sheath formation of regenerated axons at the injury/graft site. (**A**) Schematic diagram displaying the region of interest (blue squares) of myelin sheath detected in the dorsal white matter of the spinal cord injury/graft site. (**B**) and (**C**) Many new myelin sheaths (arrows in B) are visible in semi-thin sections stained by toluidine blue in the WMLT group and a few new myelin sheaths (arrow in C) are stained in the CS-OPC-N group. (**D**) The number of new myelin sheaths in spinal cord lesions in the two groups (**P < 0.01). (**E**) and (**F**) GFP $^{+}$ cells expressed MBP and wrapped NF $^{+}$ regenerating nerve fibers at the spinal cord injury/graft site (arrows in E and F). (**G**) TEM showing that regenerating axons (asterisks) were wrapped by new myelin sheaths (arrows) at the injury/graft site in the WMLT group. Data are presented as mean ± SD ($n = 3$). One-way ANOVA with an LSD-*t* test was performed. Scale bars = 10 μm in (B), (C), (E) and (F); 1 μm in (G).

sensory nerve information [21,29]. These rats displayed impaired hind limb coordination when walking on flat ground or a horizontal ladder. Motor function repair aims to guide regeneration of defective axons and promote formation of functional nerve connections. Although simple DON scaffolds and DON-OPC transplantation partially restored hind limb motor function (such as supporting body weight and coordinated motor control), the fine motor function (such as footprints of both hind limbs, and frequency of both hind limb errors) was inferior to that observed in the CS-OPC-N group, suggesting that inclusion of OPC-NT-3 contributed to an improved microenvironment for promotion of axon regeneration and remyelination. The behavioral recovery of rats in the WMLT group was superior to that observed for the CS-OPC-N group, and the hind limb gait in the WMLT group was significantly improved while the frequency of hind limb errors was reduced. Functional repair was likely improved by the myelination potential of OPCs, the LN- and NT-3-rich microenvironment, and directional guidance provided by the DON scaffold. Future behavioral testing in animals with incomplete SCI would benefit from methods like the Nokov (metric) optical 3D motion capture system that provides a more detailed evaluation of paralyzed limb support and coordination of movement [39].

4.4. Possible nerve fiber repair mechanism in WMLT

Unlike the random distribution of GFP $^{+}$ cells and the disoriented regeneration of NF $^{+}$ nerve fibers observed in the CS-OPC-N group, the GFP $^{+}$ cells in the WMLT group were evenly distributed in a straight channel, and the axons displayed a clear tendency to regenerate along the channel. The WMLT group was associated with regeneration of larger numbers of VGluT $^{+}$ nerve fibers, which may have contributed to the observed improvements in motor function [6,40], and an increase in

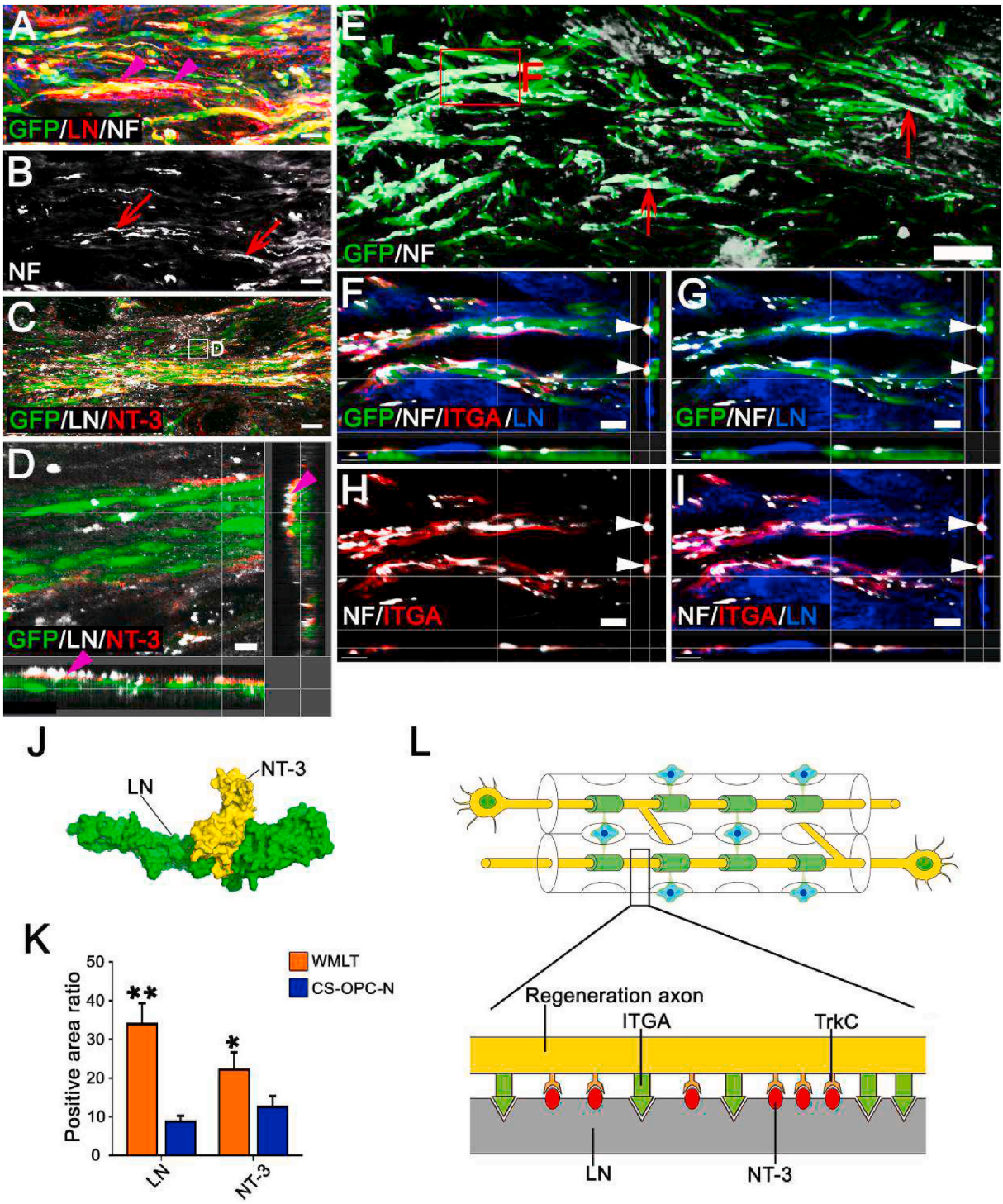

Fig. 8. Mechanism of promotion of directional nerve fiber regeneration by WMLT. (**A**) and (**B**) LN positive ECM (arrowheads in A) provided direction for GFP $^{+}$ cells and NF $^{+}$ regenerated nerve fibers (arrows in B) at the injury/graft site of an injured spinal cord. (**C**) and (**D**) NT-3 secreted by GFP $^{+}$ cells was observed tightly bound to LN (arrowheads in D). (**E**) Distribution of GFP^{+} cells and NF^{+} regenerated axons (arrows) 1 month after implantation. (**F**)–(**I**) LN interacted with NF $^{+}$ axons expressing ITGA in the WMLT implant region. NF^{+} and ITGA $^{+}$ nerve fibers were observed to regenerate and attach to LN (arrowheads). (**J**) Side view of the protein surface of NT-3 and LN. (**K**) Bar chart showing the relative intensity of LN and NT-3 in the two groups (**P < 0.01, *P < 0.05). (**L**) Schematic diagram of the mechanism by which WMLT promotes axon regeneration. LN deposited on the surface of a DON channel binds to NT-3 and promotes axon regeneration by activating TrkC on the surface of axons. LN also provides directional guidance to the regenerating axons by binding to ITGA on the axon surface. Data are presented as mean ± SD (n = 5). One-way ANOVA with an LSD-t test was performed. Scale bars = 30 μm in (A) and (B); 10 μm in (C) and (D); 100 μm in (E); 20 μm in (F)–(I).

CGRP $^{+}$ nerve fibers, which may have been responsible for the recovery in sensory perception [1]. These findings are consistent with the improved behavioral functions observed in the WMLT group compared with those in the CS-OPC-N group.

Currently, most SCI research focuses on nerve fiber regeneration. Several studies have suggested that transplantation of pre-motor interneurons or inducible pluripotent stem cell-derived neural precursor cells can promote long-distance regeneration of axons and facilitate

axonal travel across the injured area; however, functionality has not been fully restored [6,7]. We speculated that functional defects may be associated with insufficient myelination of regenerated axons under these conditions [41]. Axonal myelination in spinal cord white matter is critical for restoring function. Demyelinating diseases are associated with disruptions in motor and sensory functions [2,42]. Therefore, we attributed the increase in behavioral recovery observed in the WMLT group to improved axonal remyelination. In the transplanted area of the WMLT group, the regenerated axons were ensheathed by myelin formed by GFP $^{+}$ oligodendrocytes. Large quantities of new myelin sheath could be observed in the transplanted area using semi-thin sections and TEM. The WMLT induced NF $^{+}$ nerve fiber growth due to the enhanced microenvironment and provision of channels to direct straight axonal regeneration. The WMLT further improved motor function by supporting survival of the transplanted oligodendrocytes, which formed myelin sheaths around the regenerated axons. However, re-transecting the regenerated axons at the spinal cord injury/graft site is an excellent way to validate observations on behavioral impacts, which is a key consideration for using this scheme in future studies to verify axon regeneration and functional integration.

We also identified a linear deposition of LN on the surface of DON channels, which likely contributes to the generation of a suitable microenvironment for nerve fiber regeneration and myelination [21,43]. Many studies have demonstrated that LN is an important ECM protein that promotes nerve regeneration [20,21,44,45]. During preparation of biomaterials, LN is commonly used to coat materials to promote slow, rather than sudden, release of neurotrophic factors (such as NT-3 or BDNF) [46,47]. In this study, we found that LN was linearly deposited on the surface of DON channels and could interact with NT-3 secreted by transplanted cells to create a microenvironment rich in NT-3. Several studies have shown that NT-3 promotes nerve fiber regeneration and myelination, has anti-inflammatory effects, and inhibits excessive proliferation of astrocytes [10,15,48,49], which may account for the reduced inflammatory and astrocytic responses observed in the WMLT group as compared with the CS-OPC-N group. Notably, our results indicate that LN might provide directional guidance to regenerating axons by binding to ITGA on their surface [20,44]. Thus, NT-3 likely acts as a chemoattractant for axons and can promote axonal regeneration, while LN forms a path for axon extension via binding to ITGA [20,38]. The CS scaffold has little LN to enrich NT-3 and guide axon regeneration, which may explain the low number of straight regenerated and myelinated axons in the WMLT group as compared with the CS-OPC-N group. In future studies, WMLT should be considered for transcriptomics and proteomics analysis to identify which signaling pathways regulate axon regeneration or myelination.

5. Conclusion

In this study, WMLT was constructed using information obtained from proteomics and transcriptomics analyses. WMLT can be used as a pathological or physiological *in vitro* model to study nerve regeneration and myelination. Importantly, WMLT transplants integrate well with host spinal cord white matter, facilitating axonal regeneration and remyelination, thus effectively overcoming several barriers to directional axonal regeneration and myelination during SCI repair. In future research, humanized, gene-edited, pig-derived DON scaffolds seeded with autologous induced pluripotent stem cell-derived OPCs from patients could be used to construct WMLT for clinical SCI repair. The unique microstructure and bioactive ECM of the DON may allow for future construction of neural tissues and organoids with specific cell niches for *in vitro* studies or repair of central and peripheral nerve injuries.

Declaration of interests

The authors declare no conflict of interest.

CRediT authorship contribution statement

Bi-Qin Lai: Formal analysis, Writing – original draft, Methodology, Supervision. **Yu-Rong Bai:** Formal analysis, Writing – original draft, Methodology. **Wei-Tao Han:** Formal analysis, Methodology, Data curation. **Bao Zhang:** Formal analysis, Methodology, Data curation. **Shu Liu:** Methodology, Data curation. **Jia-Hui Sun:** Methodology, Data curation. **Jia-Lin Liu:** Methodology, Data curation. **Ge Li:** Methodology, Data curation. **Xiang Zeng:** Methodology, Data curation. **Ying Ding:** Methodology, Data curation. **Yuan-Huan Ma:** Methodology, Data curation. **Ling Zhang:** Methodology, Data curation. **Zheng-Hong Chen:** Methodology, Data curation. **Jun Wang:** Methodology, Data curation. **Yuan Xiong:** Methodology, Data curation. **Jin-Hua Wu:** Methodology, Data curation. **Qi Quan:** Methodology, Data curation. **Ling-Yan Xing:** Methodology, Data curation. **Hong-Bo Zhang:** Formal analysis. **Yuan-Shan Zeng:** Formal analysis, Writing – original draft, Supervision.

Acknowledgements

This work was supported by grants from the National Natural Science Foundation of China, Nos. 81891003 (to YSZ), 81971157 (to BQL); the National Key R&D Program of China, Nos. 2017YFA0104704 (to BQL), 2017YFA0104701 (to YSZ); the Young Elite Scientist Sponsorship Program by CAST (YESS), No. 2018QNRC001 (to BQL); the Fundamental Research Funds for the Central Universities, China, Nos. 20ykpy156 (to YHM); the 111 Project for Academic Exchange Program, China, No. B13037 (to YSZ, YD and YHM); the Natural Science Foundation of Guangdong Province, China, Nos. 2018A030310110 (to YHM), 2020A1515011537 (to YHM); the Foundation of Guangdong Province, China, No. 2017B020210012 (to YSZ and XZ); and the Start-up Foundation of Guangdong Province, China, No. 2018A030310113 (to GL).

Appendix A. Supplementary data

Supplementary data to this article can be found online at https://doi.org/10.1016/j.bioactmat.2021.10.005.

References

[1] J. Koffler, W. Zhu, X. Qu, O. Platoshyn, J.N. Dulin, J. Brock, L. Graham, P. Lu, J. Sakamoto, M. Marsala, S. Chen, M.H. Tuszynski, Biomimetic 3D-printed scaffolds for spinal cord injury repair, Nat. Med. 25 (2) (2019) 263–269.
[2] L.M. Marquardt, V.M. Doulames, A.T. Wang, K. Dubbin, R.A. Suhar, M. J. Kratochvil, Z.A. Medress, G.W. Plant, S.C. Heilshorn, Designer, injectable gels to prevent transplanted Schwann cell loss during spinal cord injury therapy, Science advances 6 (14) (2020) eaaz1039.
[3] A. Al Mamun, I. Monalisa, K. Tul Kubra, A. Akter, J. Akter, T. Sarker, F. Munir, Y. Wu, C. Jia, M. Afrin Taniya, J. Xiao, Advances in immunotherapy for the treatment of spinal cord injury, Immunobiology 226 (1) (2020) 152033.
[4] K. Xi, Y. Gu, J. Tang, H. Chen, Y. Xu, L. Wu, F. Cai, L. Deng, H. Yang, Q. Shi, W. Cui, L. Chen, Microenvironment-responsive immunoregulatory electrospun fibers for promoting nerve function recovery, Nat. Commun. 11 (1) (2020) 4504.
[5] B. Yang, F. Zhang, F. Cheng, L. Ying, C. Wang, K. Shi, J. Wang, K. Xia, Z. Gong, X. Huang, C. Yu, F. Li, C. Liang, Q. Chen, Strategies and prospects of effective neural circuits reconstruction after spinal cord injury, Cell Death Dis. 11 (6) (2020) 439.
[6] P. Assinck, G.J. Duncan, B.J. Hilton, J.R. Plemel, W. Tetzlaff, Cell transplantation therapy for spinal cord injury, Nat. Neurosci. 20 (5) (2017) 637–647.
[7] I. Fischer, J.N. Dulin, M.A. Lane, Transplanting neural progenitor cells to restore connectivity after spinal cord injury, Nat. Rev. Neurosci. 21 (7) (2020) 366–383.
[8] P. Vancamp, L. Butruille, B.A. Demeneix, S. Remaud, Thyroid hormone and neural stem cells: repair potential following brain and spinal cord injury, Front. Neurosci. 14 (2020) 875.
[9] G.J. Delcroix, E. Garbayo, L. Sindji, O. Thomas, C. Vanpouille-Box, P.C. Schiller, C. N. Montero-Menei, The therapeutic potential of human multipotent mesenchymal stromal cells combined with pharmacologically active microcarriers transplanted in hemi-parkinsonian rats, Biomaterials 32 (6) (2011) 1560–1573.
[10] B.Q. Lai, B. Feng, M.T. Che, L.J. Wang, S. Cai, M.Y. Huang, H.Y. Gu, B. Jiang, E. A. Ling, M. Li, X. Zeng, Y.S. Zeng, A modular assembly of spinal cord-like tissue allows targeted tissue repair in the transected spinal cord, Advanced science (Weinheim, Baden-Wurttemberg, Germany) 5 (9) (2018) 1800261.
[11] N. Pukos, M.T. Goodus, F.R. Sahinkaya, D.M. McTigue, Myelin status and oligodendrocyte lineage cells over time after spinal cord injury: what do we know and what still needs to be unwrapped? Glia 67 (11) (2019) 2178–2202.

[12] Q. Cao, Q. He, Y. Wang, X. Cheng, R.M. Howard, Y. Zhang, W.H. DeVries, C. B. Shields, D.S. Magnuson, X.M. Xu, D.H. Kim, S.R. Whittemore, Transplantation of ciliary neurotrophic factor-expressing adult oligodendrocyte precursor cells promotes remyelination and functional recovery after spinal cord injury, J. Neurosci. : Off. J. Soc. Neurosci. 30 (8) (2010) 2989–3001.
[13] G.J. Duncan, S.B. Manesh, B.J. Hilton, P. Assinck, J.R. Plemel, W. Tetzlaff, The fate and function of oligodendrocyte progenitor cells after traumatic spinal cord injury, Glia 68 (2) (2020) 227–245.
[14] N. Rubio, R. Rodriguez, M.A. Arevalo, In vitro myelination by oligodendrocyte precursor cells transfected with the neurotrophin-3 gene, Glia 47 (1) (2004) 78–87.
[15] Z. Yang, A. Zhang, H. Duan, S. Zhang, P. Hao, K. Ye, Y.E. Sun, X. Li, NT3-chitosan elicits robust endogenous neurogenesis to enable functional recovery after spinal cord injury, Proc. Natl. Acad. Sci. U.S.A. 112 (43) (2015) 13354–13359.
[16] X. Sun, C. Zhang, J. Xu, H. Zhai, S. Liu, Y. Xu, Y. Hu, H. Long, Y. Bai, D. Quan, Neurotrophin-3-Loaded multichannel nanofibrous scaffolds promoted anti-inflammation, neuronal differentiation, and functional recovery after spinal cord injury, ACS Biomater. Sci. Eng. 6 (2) (2020) 1228–1238.
[17] F. Sun, T. Shi, T. Zhou, D. Dong, J. Xie, R. Wang, X. An, M. Chen, J. Cai, 3D poly (lactic-co-glycolic acid) scaffolds for treating spinal cord injury, J. Biomed. Nanotechnol. 13 (3) (2017) 290–302.
[18] X.J. Wang, C.H. Peng, S. Zhang, X.L. Xu, G.F. Shu, J. Qi, Y.F. Zhu, D.M. Xu, X. Q. Kang, K.J. Lu, F.Y. Jin, R.S. Yu, X.Y. Ying, J. You, Y.Z. Du, J.S. Ji, Polysialic-acid-based micelles promote neural regeneration in spinal cord injury therapy, Nano Lett. 19 (2) (2019) 829–838.
[19] D. Joung, V. Truong, C.C. Neitzke, S.Z. Guo, P.J. Walsh, J.R. Monat, F. Meng, S. H. Park, J.R. Dutton, A.M. Parr, M.C. McAlpine, 3D printed stem-cell derived neural progenitors generate spinal cord scaffolds, Adv. Funct. Mater. 28 (39) (2018).
[20] J.H. Sun, G. Li, T.T. Wu, Z.J. Lin, J.L. Zou, L.J. Huang, H.Y. Xu, J.H. Wang, Y. H. Ma, Y.S. Zeng, Decellularization optimizes the inhibitory microenvironment of the optic nerve to support neurite growth, Biomaterials 258 (2020) 120289.
[21] Y.R. Bai, B.Q. Lai, W.T. Han, J.H. Sun, G. Li, Y. Ding, X. Zeng, Y.H. Ma, Y.S. Zeng, Decellularized optic nerve functional scaffold transplant facilitates directional axon regeneration and remyelination in the injured white matter of the rat spinal cord, Neural regeneration research 16 (11) (2021) 2276–2283.
[22] B.Q. Lai, J.M. Wang, J.J. Duan, Y.F. Chen, H.Y. Gu, E.A. Ling, J.L. Wu, Y.S. Zeng, The integration of NSC-derived and host neural networks after rat spinal cord transection, Biomaterials 34 (12) (2013) 2888–2901.
[23] S. Marques, A. Zeisel, S. Codeluppi, D. van Bruggen, A. Mendanha Falcão, L. Xiao, H. Li, M. Häring, H. Hochgerner, R.A. Romanov, D. Gyllborg, A. Muñoz Manchado, G. La Manno, P. Lönnerberg, E.M. Floriddia, F. Rezayee, P. Ernfors, E. Arenas, J. Hjerling-Leffler, T. Harkany, W.D. Richardson, S. Linnarsson, G. Castelo-Branco, Oligodendrocyte heterogeneity in the mouse juvenile and adult central nervous system, Science (New York, N.Y.) 352 (6291) (2016) 1326–1329.
[24] S.L. Wolock, R. Lopez, A.M. Klein, Scrublet: computational identification of cell doublets in single-cell transcriptomic data, Cell systems 8 (4) (2019) 281–291, e9.
[25] K. Polański, M.D. Young, Z. Miao, K.B. Meyer, S.A. Teichmann, J.E. Park, BBKNN: fast batch alignment of single cell transcriptomes, Bioinformatics 36 (3) (2020) 964–965.
[26] F.A. Wolf, P. Angerer, F.J. Theis, SCANPY: large-scale single-cell gene expression data analysis, Genome Biol. 19 (1) (2018) 15.
[27] M. Yan, Y.W. Liu, W. Shao, X.G. Mao, M. Yang, Z.X. Ye, W. Liang, Z.J. Luo, EGb761 improves histological and functional recovery in rats with acute spinal cord contusion injury, Spinal Cord 54 (4) (2016) 259–265.
[28] Z. Peng, W. Gao, B. Yue, J. Jiang, Y. Gu, J. Dai, L. Chen, Q. Shi, Promotion of neurological recovery in rat spinal cord injury by mesenchymal stem cells loaded on nerve-guided collagen scaffold through increasing alternatively activated macrophage polarization, Journal of tissue engineering and regenerative medicine 12 (3) (2018) e1725–e1736.
[29] D.O. Dias, H. Kim, D. Holl, B. Werne Solnestam, J. Lundeberg, M. Carlén, C. Göritz, J. Frisén, Reducing pericyte-derived scarring promotes recovery after spinal cord injury, Cell 173 (1) (2018) 153–165, e22.
[30] W.A. Abbas, M.E. Ibrahim, M. El-Naggar, W.A. Abass, I.H. Abdullah, B.I. Awad, N. K. Allam, Recent advances in the regenerative approaches for traumatic spinal cord injury: materials perspective, ACS Biomater. Sci. Eng. 6 (12) (2020) 6490–6509.
[31] Y. Jiang, P. Fu, Y. Liu, C. Wang, P. Zhao, X. Chu, X. Jiang, W. Yang, Y. Wu, Y. Wang, G. Xu, J. Hu, W. Bu, Near-infrared light-triggered NO release for spinal cord injury repair, Science advances 6 (39) (2020).
[32] M. Trawczynski, G. Liu, B.T. David, R.G. Fessler, Restoring motor neurons in spinal cord injury with induced pluripotent stem cells, Front. Cell. Neurosci. 13 (2019) 369.
[33] J.L. Zou, S. Liu, J.H. Sun, W.H. Yang, Y.W. Xu, Z.L. Rao, B. Jiang, Q.T. Zhu, X. L. Liu, J.L. Wu, C. Chang, H.Q. Mao, E.A. Ling, D.P. Quan, Y.S. Zeng, Peripheral nerve-derived matrix hydrogel promotes remyelination and inhibits synapse formation, Adv. Funct. Mater. 28 (13) (2018).
[34] C. Zheng, Z. Yang, S. Chen, F. Zhang, Z. Rao, C. Zhao, D. Quan, Y. Bai, J. Shen, Nanofibrous nerve guidance conduits decorated with decellularized matrix hydrogel facilitate peripheral nerve injury repair, Theranostics 11 (6) (2021) 2917–2931.
[35] P.M. Crapo, C.J. Medberry, J.E. Reing, S. Tottey, Y. van der Merwe, K.E. Jones, S. F. Badylak, Biologic scaffolds composed of central nervous system extracellular matrix, Biomaterials 33 (13) (2012) 3539–3547.
[36] X. Zeng, X.C. Qiu, Y.H. Ma, J.J. Duan, Y.F. Chen, H.Y. Gu, J.M. Wang, E.A. Ling, J. L. Wu, W. Wu, Y.S. Zeng, Integration of donor mesenchymal stem cell-derived neuron-like cells into host neural network after rat spinal cord transection, Biomaterials 53 (2015) 184–201.
[37] G. Chen, S.S. Kang, Z. Wang, E.H. Ahn, Y. Xia, X. Liu, I.M. Sandoval, F. P. Manfredsson, Z. Zhang, K. Ye, Netrin-1 receptor UNC5C cleavage by active δ-secretase enhances neurodegeneration, promoting Alzheimer's disease pathologies, Science advances 7 (16) (2021).
[38] H.M. Tuinstra, M.O. Aviles, S. Shin, S.J. Holland, M.L. Zelivyanskaya, A.G. Fast, S. Y. Ko, D.J. Margul, A.K. Bartels, R.M. Boehler, B.J. Cummings, A.J. Anderson, L. D. Shea, Multifunctional, multichannel bridges that deliver neurotrophin encoding lentivirus for regeneration following spinal cord injury, Biomaterials 33 (5) (2012) 1618–1626.
[39] Y. Zhang, E. Wang, M. Wang, S. Liu, W. Ge, Design and experimental research of knee joint prosthesis based on gait acquisition technology, Biomimetics 6 (2) (2021).
[40] H. Gezelius, A. Wallén-Mackenzie, A. Enjin, M. Lagerström, K. Kullander, Role of glutamate in locomotor rhythm generating neuronal circuitry, J. Physiol. Paris 100 (5–6) (2006) 297–303.
[41] Z. Hassannejad, A. Shakouri-Motlagh, M. Mokhatab, S.A. Zadegan, M. Sharif-Alhoseini, F. Shokraneh, V. Rahimi-Movaghar, Oligodendrogliogenesis and axon remyelination after traumatic spinal cord injuries in animal studies: a systematic review, Neuroscience 402 (2019) 37–50.
[42] J.R. Plemel, J.A. Stratton, N.J. Michaels, K.S. Rawji, E. Zhang, S. Sinha, C. S. Baaklini, Y. Dong, M. Ho, K. Thorburn, T.N. Friedman, S. Jawad, C. Silva, A. V. Caprariello, V. Hoghooghi, J. Yue, A. Jaffer, K. Lee, B.J. Kerr, R. Midha, P. K. Stys, J. Biernaskie, V.W. Yong, Microglia response following acute demyelination is heterogeneous and limits infiltrating macrophage dispersion, Science advances 6 (3) (2020), eaay6324.
[43] L.X. Deng, N.K. Liu, R.N. Wen, S.N. Yang, X. Wen, X.M. Xu, Laminin-coated multifilament entubulation, combined with Schwann cells and glial cell line-derived neurotrophic factor, promotes unidirectional axonal regeneration in a rat model of thoracic spinal cord hemisection, Neural regeneration research 16 (1) (2021) 186–191.
[44] R.I. Nichol, K.M. Hagen, D.C. Lumbard, E.W. Dent, T.M. Gómez, Guidance of axons by local coupling of retrograde flow to point contact adhesions, J. Neurosci. : Off. J. Soc. Neurosci. 36 (7) (2016) 2267–2282.
[45] A.J. Matamoros, V.J. Tom, D. Wu, Y. Rao, D.J. Sharp, P.W. Baas, Knockdown of fidgetin improves regeneration of injured axons by a microtubule-based mechanism, J. Neurosci. : Off. J. Soc. Neurosci. 39 (11) (2019) 2011–2024.
[46] Q. Zhang, S. Yan, R. You, D.L. Kaplan, Y. Liu, J. Qu, X. Li, M. Li, X. Wang, Multichannel silk protein/laminin grafts for spinal cord injury repair, J. Biomed. Mater. Res. 104 (12) (2016) 3045–3057.
[47] J. Ruzicka, N. Romanyuk, K. Jirakova, A. Hejcl, O. Janouskova, L.U. Machova, M. Bochin, M. Pradny, L. Vargova, P. Jendelova, The effect of iPS-derived neural progenitors seeded on laminin-coated pHEMA-MOETACl hydrogel with dual porosity in a rat model of chronic spinal cord injury, Cell Transplant. 28 (4) (2019) 400–412.
[48] M.E. Yalvac, W.D. Arnold, C. Braganza, L. Chen, J.R. Mendell, Z. Sahenk, AAV1. NT-3 gene therapy attenuates spontaneous autoimmune peripheral polyneuropathy, Gene Ther. 23 (1) (2016) 95–102.
[49] G. Li, B. Zhang, J.H. Sun, L.Y. Shi, M.Y. Huang, L.J. Huang, Z.J. Lin, Q.Y. Lin, B. Q. Lai, Y.H. Ma, B. Jiang, Y. Ding, H.B. Zhang, M.X. Li, P. Zhu, Y.Q. Wang, X. Zeng, Y.S. Zeng, An NT-3-releasing bioscaffold supports the formation of TrkC-modified neural stem cell-derived neural network tissue with efficacy in repairing spinal cord injury, Bioact. Mater. 6 (11) (2021) 3766–3781.